Independent Components Analysis of Local Field Potential Sources in the Primate Superior Colliculus

by

Yu Liu

B.S. in Telecommunication Engineering,

Nanjing University of Posts and Telecommunications, 2017

Submitted to the Graduate Faculty of

the Swanson School of Engineering in partial fulfillment

of the requirements for the degree of

Master of Science

University of Pittsburgh

2019

UNIVERSITY OF PITTSBURGH

SWANSON SCHOOL OF ENGINEERING

This thesis was presented

by

Yu Liu

It was defended on

July 17, 2019

and approved by

Ahmed Dallal, Ph.D., Assistant Professor, Department of Electrical and Computer Engineering

Neeraj Gandhi, Ph.D., Professor, Department of Bioengineering

Amro El-Jaroudi, Ph.D., Associate Professor, Department of Electrical and Computer Engineering

Zhi-Hong Mao, Ph.D., Professor, Department of Electrical and Computer Engineering

Thesis Advisors: Ahmed Dallal, Ph.D., Assistant Professor, Department of Electrical and Computer Engineering,

Neeraj Gandhi, Ph.D., Professor, Department of Bioengineering

Independent Components Analysis of Local Field Potential Sources in the Primate Superior Colliculus

Yu Liu, M.S.

University of Pittsburgh, 2019

When visually-guided eye movements (saccades) are produced, some signal-available electrical potentials are recorded by electrodes in the superior colliculus (SC), which is ideal to investigate communication between the different layers due to the laminar organization and structured anatomical connections within SC. The first step to realize this objective is identifying the location of signal-generators involved in the procedure. Local Field Potential (LFP), representing a combination of the various generators measured in the vicinity of each electrodes, makes this issue as similar as blind source separation problem. Thus, Independent Component Analysis (ICA) is proposed to analyze the specific spatial and temporal properties of LFP recorded in Rhesus monkeys performing a standard delayed saccade task. After being preprocessed, the LFP data is decomposed into two parts: mixing matrix and independent component (IC). The LFPs are binned into segments, and the ICs and their corresponding mixing weights are computed for each epoch.

We also compared our results against current source density (CSD) techniques, which relies on the second spatial derivative of the mixing coefficients computed with a Laplacian of Gaussian kernel. We then reconstructed the CSD that corresponds to each component by multiplying that IC by the computed derivative of its coefficients. To identify the dominant ICs, we performed correlation analysis between each CSD reconstructed via a single IC against the ground truth CSD (the second spatial derivative of the raw LFP) and we kept only those ICs with a correlation score exceeding a predefined threshold. These dominant ICs correspond to the current generators in this time window, and the spatial distribution of the coefficients defines the depth at which this sink originates. Our analysis indicates that the correlation between the IC based reconstruction and the ground truth CSD exceeds 90% in best. We consistently identified 2-3 generator sites, mostly confined near the boundary of superficial and intermediate layers. The strongest modulations occurred slightly after saccade

onset and in response to target onset. Thus, the ICA method can accurately reconstruct the CSD, as well as identify and quantify the origin of current sinks.

Table of Contents

1.0 Introduction and Background 1

1.1 Background Of LFP 1

1.1.1 Roadmap of LFP Technology 2

1.1.2 Mathematical Models of LFP 3

1.2 Comparison to Other Brain Signals 8

1.3 Main Contributions 9

1.4 Organization of the Thesis 11

2.0 Data Acquisition 12

2.1 Animals Preparation 12

2.2 Neurophysiological Recording and Data Collection 13

2.3 Acknowledgment 14

3.0 Localizing Source generators 15

3.1 Current Source Density Analysis 15

3.2 Independent Components Analysis 18

3.2.1 Mathematical Analysis of ICA 19

3.2.2 Independence 20

3.2.3 The Procedure of ICA 22

3.2.4 Estimation Algorithm of ICA 22

3.2.4.1 Maximization of nongaussianity 23

3.2.4.2 Minimization of Mutual Information 25

3.2.4.3 Infomax Method 26

3.2.4.4 Maximum Likelihood Estimation 27

3.3 FastICA 28

3.4 Source Clustering Algorithm 30

4.0 Neurophysiological Analysis 32

4.1 Preprocessing data 32

4.2 Results and Discussions 33
4.2.1 Simulation data 33
4.2.2 Global Time Scale 37
4.2.3 Local Time Scale 43
4.2.4 Supplemental Experiments 49
4.2.4.1 BB080415 49
4.2.4.2 BU080918 56
4.3 Conclusion and Future Work 56
4.3.1 Conclusion 56
4.3.2 Future Work 63
Bibliography 64

List of Tables

1 Similarity between Original and Reconstructed CSD on Simulation Data Sets 37

2 Similarity between Original and Reconstructed CSD on BL071717 49

3 Similarity between Original and Reconstructed CSD on BB080415 49

4 Similarity between Original and Reconstructed CSD on BU080918 56

List of Figures

1 Electrodes in Cortical Neuron Tissue 3

2 (a) simultaneous recordings from the LFP, ECoG and scalp EEG (b) simultaneous recorded LFP(blue), scalp EEG(red) and multi-unit activity spikes(green) in different depths (c) simultaneous recorded MEG(black) and scalp EEG(red) (d) simultaneous recorded LFP in superficial and deep layers of the motor cortex [18–21] 10

3 Monkey Performing Saccade Task 13

4 The Multivariate Distribution of Two independent Gaussian Variables 21

5 The Flow Chart of ICA 22

6 The Flowchart of Updating Weights 29

7 Time Blocks on Timeline 32

8 Four Different Simulation Datasets 34

9 (a) LFP of Sampled Simulated Data (b) CSD of Sampled Simulated Data (c) Mixing Columns (d) 2^{nd} Derivative of Mixing Columns (e) Independent Components (f) Reconstructed CSD 35

10 (a) LFP of Sampled Simulated Data (b) CSD of Sampled Simulated Data (c) Mixing Columns (d) 2^{nd} Derivative of Mixing Columns (e) Independent Components (f) Reconstructed CSD 38

11 (a) LFP of Sampled Simulated Data (b) CSD of Sampled Simulated Data (c) Mixing Columns (d) 2^{nd} Derivative of Mixing Columns (e) Independent Components (f) Reconstructed CSD 39

12 (a) LFP of Sampled Simulated Data (b) CSD of Sampled Simulated Data (c) Mixing Columns (d) 2^{nd} Derivative of Mixing Columns (e) Independent Components (f) Reconstructed CSD 40

13 (a) LFP of Dataset (b) LFP of Dataset with Step Lines (C) CSD of Dataset (d) CSD of Dataset with Step Lines 41

14 (a) Independent Components in Global Scale (b) Spectral Power of Peaking IC (c) Spectral Power of Residual IC 42
15 (a) CSD epochs of target onset block (b) reconstructed CSD epochs of target onset block 45
16 (a) CSD epochs of saccade task epochs (b) reconstructed CSD epochs of saccade task block 46
17 (a) 2^{nd} Derivative Coefficients of Epochs in Target Onset Block (b) 2^{nd} Derivative Coefficients of Epochs in Saccade Task Block 47
18 (a) ICs of Epochs in Target Onset Block (b) ICs of Epochs in Saccade Task Block 48
19 (a) LFP of Dataset (b) LFP of Dataset with Step Lines (C) CSD of Dataset (d) CSD of Dataset with Step Lines 50
20 (a) Independent Components in Global Scale (b) Spectral Power of Peaking IC (c) Spectral Power of Residual IC 51
21 (a) CSD epochs of target onset block (b) reconstructed CSD epochs of target onset block 52
22 (a) CSD epochs of saccade task epochs (b) reconstructed CSD epochs of saccade task block 53
23 (a) 2^{nd} Derivative Coefficients of Epochs in Target Onset Block (b) 2^{nd} Derivative Coefficients of Epochs in Saccade Task Block 54
24 (a) ICs of Epochs in Target Onset Block (b) ICs of Epochs in Saccade Task Block 55
25 (a) LFP of Dataset (b) LFP of Dataset with Step Lines (C) CSD of Dataset (d) CSD of Dataset with Step Lines 57
26 (a) Independent Components in Global Scale (b) Spectral Power of Peaking IC (c) Spectral Power of Residual IC 58
27 (a) CSD epochs of target onset block (b) reconstructed CSD epochs of target onset block 59
28 (a) CSD epochs of saccade task epochs (b) reconstructed CSD epochs of saccade task block 60

29 (a) 2^{nd} Derivative Coefficients of Epochs in Target Onset Block (b) 2^{nd} Derivative Coefficients of Epochs in Saccade Task Block 61
30 (a) ICs of Epochs in Target Onset Block (b) ICs of Epochs in Saccade Task Block 62

1.0 Introduction and Background

When visually-guided eye movements (saccades) are produced, some signal-available electrical potentials are recorded by electrodes along the axis of superior colliculus (SC), which makes it ideal to investigate communication between the different layers due to the laminar organization and structured anatomical connections within SC. The first step to realize this objective is identifying the location of signal-generators during the procedure. Local Field Potential (LFP), representing a combination of the various generators measured in the vicinity of each electrodes, makes this issue as similar as blind source separation problem. Thus, Independent Component Analysis (ICA) is proposed to analyze the specific spatial and temporal properties of LFP recorded in Rhesus monkeys performing a standard delayed saccade task. After being preprocessed, the LFP data is decomposed into two parts: mixing matrix and independent component (IC). Then the results could be compared against the Current Source Density (CSD) Method, which depends on the spatial second derivatives on the LFP data. Finite difference approximation is employed on the coefficients and those resultant second derivatives will be multiplied by IC to reconstruct CSD figures. After bootstrapping and correlation analysis, it is found that there exist fixed generators during the repeated experiments. The selected ICs contribute to a reduced reconstruction CSD figures, which own high correlation with raw CSD figures. And those reconstructed figures are affected by less background noise and volume conduct activities as well. Thus, the ICA method can accurately reconstruct the CSD, as well as identifying and quantifying the origin of current sinks.

1.1 Background Of LFP

The Local Field Potential (LFP) is the electrical potentials in the extracellular space around neurons, which has specific spatial and temporal properties. It is signal accessible and could be recorded by one single electrode or multi-electrodes array based on different

recording configurations. The LFPs has been modeled by various classes of modeling schemes which own the specific spatial and temporal properties in the past few decades.

1.1.1 Roadmap of LFP Technology

As early as 1875, it was the first time to record electrical signals from cortical surfaces of animals, which is 50 years before the advent of electroencephalography [1]. The subsequent series of related work reveals the fact that the high-frequency part of the recordings, which is above 500Hz, represents the information of spike activity around the electrodes. By contrast, the signal form the low-frequency part, which is below 500Hz, shows to be obscure to interpret the underlying neuron activity, even if it is called as 'Local Field Potential'. In 1950s, Current Source Density (CSD) analysis was introduced to process LFP signals, raising widely interests in this field in the following decades [2–5].

In the recent years, the research on LFP has reached to a new level due to the growing ability to record high-density signals from multi-electrodes across areas and laminae [6, 7]. During the long-standing development, the LFP has gradually been seen as a promising signal as the spikes. Comparing to the spikes, the LFP shows the advantages in two aspects. First, the LFP could capture an integrative synaptic process rather than spike activities of a few neurons alone. Second, in the chronic recordings, the LFP is more accessible and stable than the spikes. Thus, several studies have used LFPs to investigate cortical network mechanisms involved in sensory processing, motor planning and higher cognitive processes, including attention, memory and perception [8].

However, these advantages also brought a new challenge for the LFP analysis. Since the LFP is contributed by a small population of neuron activities, it is more difficult to interpret neuronal procedure due to the cancellation effect by different neurons. This ambiguity could be resolved, at least in part, by improving the computational methods of analysis. To achieve this goal, disambiguating different neuron contributions from the raw LFP data, two inspired models for computational neuroscience have been designed.

The models of LFP represents the understanding of 'measurement physics' [8] of the LFP data, which means how to understand the link between neuron activities and the data

measured. The argument of the modelling is focused on the relationship of neural currents and the potentials. Based on the volume conduct theory, the "forward-modelling scheme" is well-founded, where "forward" denotes that transmembrane neuron currents model the extracellular potentials. In contrast, 'inverse-modeling scheme' is established on the case where neural currents is estimated from the recorded potentials. By employing the above tools, it is pursuable to investigate the link between potentials varying and underlying neuron activities.

1.1.2 Mathematical Models of LFP

Extracellular potentials arise from transmembrane currents passing through cellular membranes in the vicinity of the electrode [8]. As mentioned above, to disambiguate the framework of neurons, various modeling schemes were well established in the past decades to understand the biophysical origins inside. Based on the theory used to model biophysical mechanism, schemes are divided into "forward" and "inverse" modeling schemes.

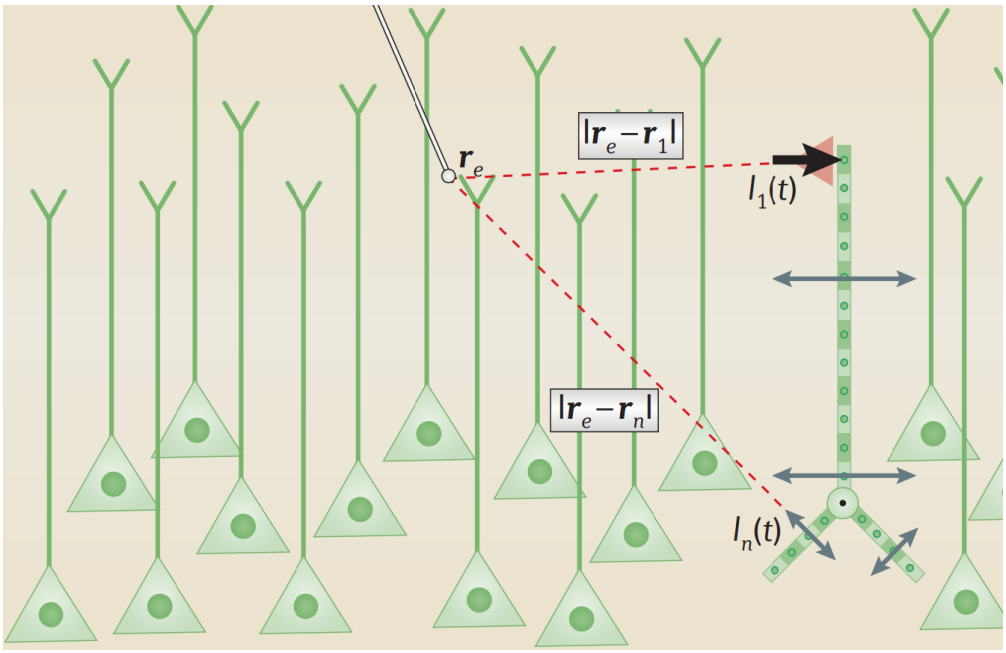

Figure 1: Electrodes in Cortical Neuron Tissue [8]

The simplest way to mold the extracellular medium is to consider it as a kind of purely resistive or ohmic medium without any capacitive component. In this case, synaptic inputs appear to be the most dominant contribution to the LFP, which follows the volume conductor theory, where extracellular medium is considered as stereoscopic continuum conductivity whose electrical potentials are raised by cellular transmembrane currents. Starting from Ohm's Law and combining with the law of current conservation, the extracellular potential Φ could be described as:

$$\Phi(r_e) = \frac{1}{4\pi\sigma} \sum_{n=1}^{N} \frac{I_n}{|r_e - r_n|} \tag{1.1}$$

Here, I_n denotes the transmembrane currents and r_e and r_n denotes the position of electrodes and current sources, which will be summed up to N components. Conductivity σ represents the conductivity of extracellular potential. From the Figure 1, the distance between electrodes and sources is vectorizable and it could be replaced by vector r. Thus, the equation to generate potential could be changed into:

$$\Phi(r_e) = \frac{1}{4\pi\sigma} \sum_{j=1}^{N} \frac{I_j}{r_j} \tag{1.2}$$

If assuming the far away reference $\Phi(\infty) = 0$, this equation could also be derivate from Maxwell-Gauss Law $\nabla \cdot \vec{D} = \rho$. If the distance reaches to a large enough size compared to the source, this expression could capture much more effects. Eq.(1.2) is widely used to model extracellular potentials since early models [9] to modern models [10–13].

In general, this scheme is limited by a set of assumptions and approximations [8], including: (1) the employment of quasi static approximation of Maxwell's equations in which electrical and magnetic fields are effectively decoupled (2) assuming that there is no capacitive capability for the extracellular medium so that its conductivity will be ohmic (3) frequency-independency (4) isotropic and homogeneous medium. These limitations make the "forward-modelling scheme" a "standard" model.

To go beyond the limitations above, a relatively real scheme was proposed to deal with those cases in which the extracellular space around neurons is not homogenous. The variation of conductivity will be consistent for the extracellular medium and the continuous change will lead to an unacceptability for the former 'forward modelling' scheme. To be adapted

for this situation, it is necessary to start from the first principle of Maxwell's equation, as done in the previous work [14]. The core of is scheme is to assume the electrical parameters follows the spatial variation along with the medium.

If a medium is considered as constant magnetic permeability, uniting the Maxwell-Gauss law $\left(\nabla \cdot \vec{D} = \rho^f\right)$ and Ampere-Maxwell law $\left(\nabla \times \frac{\vec{B}}{\mu} = \vec{j}^f + \frac{\partial \vec{D}}{\partial t}\right)$ could give back the equations group below,

$$\begin{cases} \nabla \cdot \vec{D} = \rho^f \\ \nabla \cdot \vec{j}^f + \frac{\partial \rho^f}{\partial t} = 0 \end{cases} \tag{1.3}$$

where $\vec{D}$, $\vec{j}^f$ and ρ^f are representing the electric displacement, the free-charge current density, and free-charge charge density in the medium surrounding the sources respectively.

For a linear medium, the electric displacement $\vec{D}$ and the current density $\vec{j}^f$ have a specific relationship with the electric field $\vec{E}$:

$$\vec{D}\left(\vec{x}, t\right) = \int_{-\infty}^{\infty} \varepsilon\left(\vec{x}, \tau\right) \vec{E}\left(\vec{x}, t-\tau\right) d\tau \tag{1.4}$$

and

$$\vec{j}\left(\vec{x}, t\right) = \int_{-\infty}^{\infty} \sigma\left(\vec{x}, \tau\right) \vec{E}\left(\vec{x}, t-\tau\right) d\tau \tag{1.5}$$

In this case, the value curves of electrical parameters σ and ε are separated into "microscopic" blocks. According the convolution property of Fourier Transformation, the convolution in the time domain would be turned into the multiplication in the frequency domain:

$$f(t) * g(t) \leftrightarrow f(\omega) * g(\omega) \tag{1.6}$$

Thus, Eq.(1.4) and Eq.(1.5) in the frequency domain will be the transformed to: $\vec{D}_\omega = \varepsilon_\omega \vec{E}_\omega$ and $\vec{j}_\omega = \sigma_\omega \vec{E}_\omega$, where $\omega = 2\pi f$ and f is the frequency. For the electrical parameters under the frequencies lower than 1kHz, σ and ε could be treated constant and independent of frequency. The equations above are equal to: $\vec{D}_\omega = \varepsilon \vec{E}_\omega$ and $\vec{j}_\omega = \sigma \vec{E}_\omega$.

Given the limited precision level of 'microscopic', assumption that $\nabla \times \vec{E} \approx 0$ and $\vec{E} = -\nabla\Phi$ for the frequency lower than 1kHz could be helpful for the complex Fourier transformation of Eq.(1.3):

$$\begin{cases} \nabla \cdot \left(\varepsilon\left(\vec{x}\right) \nabla \Phi_\omega\right) = -\rho_\omega^f \\ \nabla \cdot \left(\sigma\left(\vec{x}\right) \nabla \Phi_\omega\right) = i\omega\rho_\omega^f \end{cases} \tag{1.7}$$

Consequently, the united equations group could be written as:

$$\nabla \cdot ((\sigma + i\omega\varepsilon)\nabla\Phi_\omega) = 0 \tag{1.8}$$

The Eq.(1.8) is the dominant idea to generate the LFP in the inhomogeneous medium as previous work [14], which is sufficient to simulate the propagation of extracellular potentials with the frequency-dependent electrical parameters. Once the extracellular medium is homogeneous, this equation could be reduced to the Laplace equation where $\nabla^2\Phi_\omega = 0$.

The various spatial profiles of the conductivity σ and permittivity ε around neurons contributes to the function of Φ_ω, varying in space. After going through a low-pass filter, the fast frequencies are attenuated much more strongly than the low the frequencies in the propagation. Finally, the electrical potential is modelled by

$$\Phi_\omega(R) = \frac{I_\omega^f}{4\pi\sigma(R)} \int_R^\infty \frac{1}{r^2} \cdot \frac{\sigma(R) + i\omega\varepsilon(R)}{\sigma(r) + i\omega\varepsilon(r)} dr \tag{1.9}$$

Here,

$$I_\omega^f = I_m(\omega)\frac{\sigma(R)}{\sigma(R) + i\omega\varepsilon(R)} \tag{1.10}$$

and it is the free-charge current described in Fourier space. I_m is the membrane current of the source, $\sigma(R)$ and $\varepsilon(R)$ is the electrical conductivity and electrical permittivity of the membrane varying along the distance away from the source.

Another approach to simulate those electrical parameters under the changing is to compute them via a "macroscopic" scale, in which σ and ε are considered as the average value of the mixture of different medium such as fluid or membrane.

To define this macroscopic electrical parameters, ε^M and σ^M , the volume parameter V is used to describe in frequency domain:

$$\varepsilon_\omega^M(\vec{x}) = \langle \varepsilon_\omega(\vec{x}) \rangle_{|V} = f(\vec{x}, \omega) \tag{1.11}$$

and

$$\sigma_\omega^M(\vec{x}) = \langle \sigma_\omega(\vec{x}) \rangle_{|V} = g(\vec{x}, \omega) \tag{1.12}$$

Assuming the order of the volume is up to one thousand cubic microns, which is far smaller than the volume of the cortex to ensure that the value of electrical parameters could be determined by the position in cortex:

$$\langle \overrightarrow{j^{total}} \rangle_{|V} (\vec{x}, t) = \int_{-\infty}^{\infty} \sigma^M(\tau) \langle \vec{E} \rangle_{|V} (\vec{x}, t-\tau)\, d\tau + \int_{-\infty}^{\infty} \varepsilon^M(\tau) \frac{\partial \langle \vec{E} \rangle_{|V}}{\partial t} (\vec{x}, t-\tau)\, d\tau \qquad (1.13)$$

In the right of the Eq.(1.13), the first integrality represents the "dissipative" contribution and the second integral term describes the "reactive" contribution, which is reacting from the medium. In this equation, the relationship of electrical parameters σ, and ε in the time domain integrated the physical effects such as diffusion, reactive and capacitive phenomena [15]. Thus, in the frequency domain, the relationship could be written as the following equation:

$$\langle \overrightarrow{j^{total}} \rangle_{|V} = \left(\sigma_\omega^M + i\omega \varepsilon_\omega^M \right) \langle \vec{E}_\omega \rangle_{|V} \qquad (1.14)$$

Assuming the medium is uniform inside the "macroscopic" block, it has $\nabla \cdot \langle \overrightarrow{j^{total}} \rangle_{|V} = 0$ and $\langle \vec{E}_\omega \rangle = -\nabla \langle \Phi_\omega \rangle$. And the Eq.(1.14) could be transformed into:

$$\nabla \cdot \left(\left(\sigma_\omega^M + i\omega \varepsilon_\omega^M \right) \nabla \langle \Phi_\omega \rangle_{|V} \right) = 0 \qquad (1.15)$$

This equation gives a similar model as the "microscopic" model, which is described in Eq.(1.8). This form invariance allows more phenomena, like surface polarization or iconic, to be introduced in the further computation.

In this section, three formalisms used to model the LFP are reviewed. The first formalism, mostly based on Coulomb's law, defines the potentials as the response of a set of current sources in the homogenous medium. The second formalism is focused on the specific case of inhomogeneous medium, which leads to a strong dependence on the position. In this case, extracellular potentials are derived from the principles of Maxwell equation directly. Another third formalism measure the brain tissue in a large scale, in which the electrical parameters are considered as constant but are also the results of mixing the various medium in a "macroscopic" filed.

1.2 Comparison to Other Brain Signals

Different from the electroencephalogram (EEG) signals, which are recorded at the surface of the head using macro-electrodes, LFP recordings are taken from the extracellular medium around neurons with micro-electrodes made by different types of martials (metal, silicon, glasses, etc.). Compared to EEG signals, it is commonly thought that LFP samples only a relatively localized population of neurons, which is scaled into about one micrometer or even a few hundred microns. In contrast, EEG signals could sample a much larger population of neurons, reaching to several centimeters. Despite of the difference, there exist similar types of neuron oscillations displayed by LFP and EEG.

Magnetoencephalography (MEG) is the tiny magnetic fields measured outside the skull from currents generated by the neurons by superconducting quantum interference devices [16]. As EEG, MEG signals are non-invasively recorded as well. Unlike EEG, MEG has a higher spatiotemporal resolution and is less dependent on the conductivity of the extracellular medium as magnetic signals than EEG. The characteristic of magnetic signals also leads to a totally different appearance of the frequency-versus-power relationship, typically in high-frequency bands because EEG signals are more easily affected by various extracellular medium.

Electrocorticography (ECoG) records the electrophysiology activities directly from superficial surfaces of the cerebral cortex directly by the electrodes. This method could help avoid medium such as skulls or tissues from distorting the electrical signals recorded, which leads to a relatively higher spatial resolution by improving the materials of the electrodes.

As mentioned above, LFP is the low-frequency part of the electrical signals from the cortical surface. By contrast, the high-frequency part is widely called multi-unit activity (MUA), which is weighted sum over transmembrane currents in soma region. As similar as LFP, MUA is accumulated by a little population of neurons, which have their own effect on the population signals separately. Thus, MUA is challenging to dissolve the ambiguity of the underlying neuron activities either. In some analysis, MUA could be combined with LFP to tell the fact of neural activities.

Different with the above purely electrical signals, voltage-sensitive dye imaging (VSDI) method gives an optical detection of voltage varying on the membrane. Comparing to LFP, VSDI has significant advantages and limitations. The major benefit is that VSDI directly measures the transmembrane voltage changes locally instead of extracellular potentials. But it also means that the measurement could only represent surface events and is easily influenced by cell membrane activities, which leads to a low signal-to-noise ratio as other optical probe-based methods [17]. In the Figure 2, it illustrates some properties of the brain signals mentioned above.

1.3 Main Contributions

In this thesis we study the use of independent component analysis to decompose the LFP signals recorded from Rheuse monkeys. The aim of the study is to identify and quantify the current source generators within the superior colliculus. We summarize our main contributions as follows:

a) We apply ICA on the simulated data under noise-free conditions to study the relationship between mixing vectors, independent components, LFP signals, and the loci of the current sinks.

b) We reconstruct LFP signals using independent components and their corresponding mixing matrix to demonstrate the ability of ICA in denoising the original LFPs and getting rid of some undesirable effects, like volume conduction.

c) We locate the current source generators and study their activities during the task; by relating the mixing matrix and independent components extracted by ICA.

d) We reconstruct the CSD signals using the independent components and the second spatial derivative of their coefficients. Then, we compare our results against the standard method of estimating the CSD signals to prove the efficiency and accuracy of our approach.

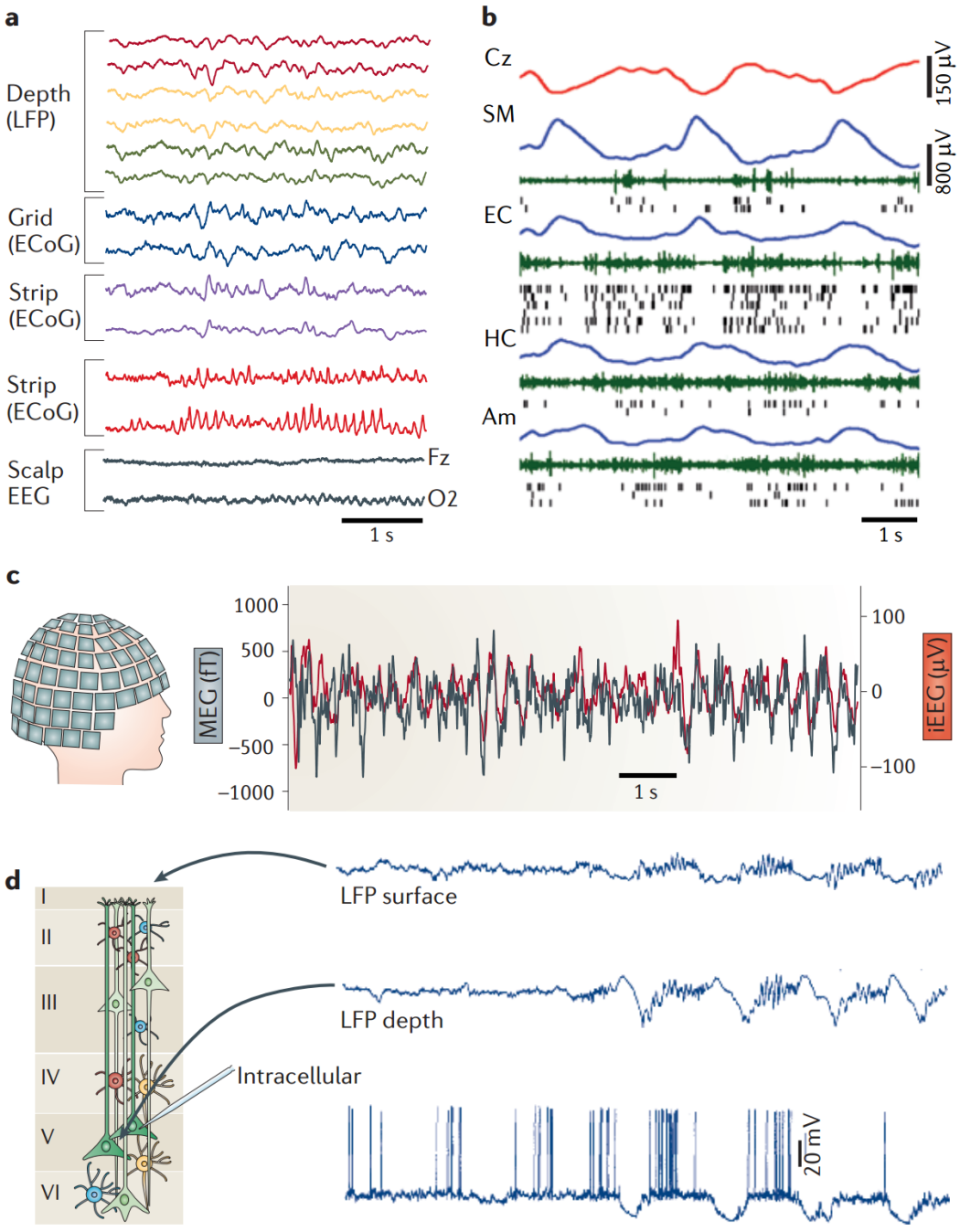

Figure 2: (a) simultaneous recordings from the LFP, ECoG and scalp EEG (b) simultaneous recorded LFP(blue), scalp EEG(red) and multi-unit activity spikes(green) in different depths (c) simultaneous recorded MEG(black) and scalp EEG(red) (d) simultaneous recorded LFP in superficial and deep layers of the motor cortex [18–21]

1.4 Organization of the Thesis

The rest of the paper is organized as the following: In Chapter 2, we explain the procedure of acquiring the data from moneys. In Chapter 3, we review the two directions of locating and quantifying source generators, traditional CSD analysis and ICA combined with correlation clustering. In Chapter 4, we present and discuss the results of neurophysiological analysis and the regular patterns under covered. Finally, we conclude the paper and propose directions for future work in Chapter 5.

2.0 Data Acquisition

In the our experiments, to record animal LFP signals from the superior colliculus, three male Rhesus macaque monkeys, names as BB, BL and BU, respectively, were used as subjects. Figure 3 summarizes the data acquisition experiment.

2.1 Animals Preparation

Three male Rhesus monkeys (*macaca mulatta*) served as subjects for the data reported here. Each animal was instrumented under aseptic conditions with a head post and a chamber over a craniotomy. The head post was used to restrain the animal's head during experiments, while the chamber provided access for an electrode that can be lowered into the brain. The chamber was tilted 40° posteriorly in the sagittal plane to ensure that the probe penetrations were approximately normal to the SC surface. Both SC could be accessed from the same chamber.

After allowing approximately 1 month for recovery from surgery, each animal was prepared for experimentation. It was trained to enter a 'primate chair'. The chair with the animal in it were rolled to the laboratory. Its head was restrained with the head post, and an infra-red illuminator and hot mirror combination was situated to track eye position. As shown in Figure 3, the animal faced a visual display (LCD monitor) that displayed dots that served as visual cues for eye movement tasks ([13]). At the beginning of each trial, a 'fixation point' was illuminated at the center of the screen. Once this condition is achieved, a second spot of light is presented in the visual periphery. The fixation point remained on for another 500-1000 ms and only when it was extinguished did the animal have the permission to make a saccade to the target in the periphery. The animal was given 400 ms to complete the movement, which resulted in delivery of a liquid reward (water). If any of these requirements are not fulfilled, the trail was aborted. Eye movements and neural activity were recorded while the animal performed these tasks.

2.2 Neurophysiological Recording and Data Collection

In the experiments, we used two kinds of laminar probes (16 channels or 24 channels, $150\mu m$ inter-contact distance, $300\mu m$ diameter, $1M\Omega$ independence for each channels) to record neural activities [28]. During the procedure of setting the probes, we follow the order, form one unit detected to multiple units detected. Once one channel had detected the neural activity, the ability to evoke a saccade are measured by delivering the biphasic electrical stimulation to the deepest contact. When we had verified that we had reached to the intermediate layer of SC, the probes would be placed more deeply to maximize the number of electrodes detected multi-unit activities. Electrical stimulation was delivered to different channels for two aims, estimating the average vector and gauging the similar properties across the depths of the saccades qualitatively.

After setting up the electrodes, the neurophysiological signals were recorded by Scout data acquisition system, which recorded the timing of all trial events and raw neural activity simultaneously from the beginning to the end of trials. For each channel, after going through different filter, the raw data could be divided into two parts. Going through the low pass filter at 250Hz, we could get the local filed potentials from the raw data. Going through the high pass filter at 250Hz and using the threshold at the 3.5 times the RMS, the raw activity was parsed into spiking activity, which is from multiple units in the vicinity of each electrode [28].

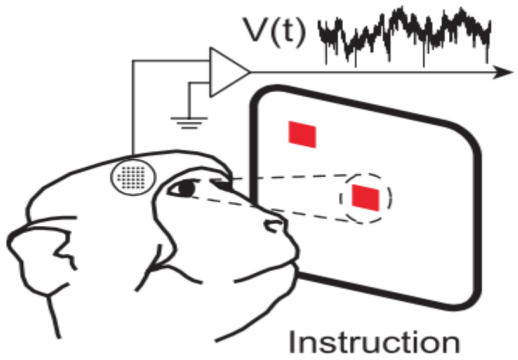

Figure 3: Monkey Performing Saccade Task

2.3 Acknowledgment

All experimental and surgical procedures are approved by the Institution Animal Care and Use Committee of the University of Pittsburgh and are following the U.S. Public Health Service policy on the human care and use of laboratory animals.

3.0 Localizing Source generators

In this chapter, two different approaches for localizing source generators are discussed. First, we review the traditional CSD analysis, followed by our proposed ICA-Clustering method.

3.1 Current Source Density Analysis

Current Source Density (CSD) analysis is a class of methods used to analyze the extracellular potentials recorded by electrodes, which aims to measure the current sources inside the potentials. Usually, it is employed on those field potentials in the low-frequency part, especially suitable for LFP.

During the formation of the extracellular potentials, the places where the current is entering or leaving the cells are called "sources" or "sinks". Due to the long-range property of the electric field, the LFP could be observed hundreds of millimeters away from the sources and sinks, which makes "local" field potentials sometimes inaccurate [22]. To eliminate this misnomer, CSD analysis is proposed as an extension to the LFP, which is helpful to locate the sources underneath the electrical potentials recorded.

When positive currents enter the cells, speaking of current sink, it corresponds to negative CSD. And when negative currents enter the cells (positive currents leave the cells), speaking of current sinks, it corresponds to positive CSD. While plotting the figures of CSD, some researchers prefer to denote current sources by red and current sinks by blue according to the sign of CSD. At the meanwhile, there is a number of researchers preferring an opposite opinion. They use red color ("hot spot") for current sinks and blue color for current sources because negative CSD is observed for excitatory synaptic stimulation in practice. These two opposite conventions are both widely used.

As an "inverse" problem of "LFP", aiming to identify the net current sources that contributes to the LFP from the LFP data, CSD certainly owns some physical relationship

with the LFP. As a quantity representing the volume density of the net current conducting among the extracellular, CSD assume conductivity as infinite, homogenous and isotropic conductive medium, similar as the "forward-model" scheme mentioned above. Consider a distant current source relative to linearly and equally spaced electrodes in this ideal medium. Each electrode could detect a part of the contribution from that distant source to the filed potentials. Thus, the difference between the electrodes could be seen the indication. If the voltage between per electrode is small, it indicates that the field could be attributed to a distant source. By contrast, if the voltage at the electrodes are unequal and the difference magnitude of this derivative is large, it indicates a local origin of the current. At the meanwhile, the current flow between two electrodes could be calculated from the voltage difference, applying Ohm's law. Once the conductance of brain tissue is accessible [23], it is possible to figure out the exact location of the sources and sinks. Similar as the derivation of the various models of the LFP, the physics behind the relation between the CSD and the LFP could also be described in mathematic derivation. Since the basic CSD assumption is the ideally homogenous medium, the equation used to measure the filed potentials in the "forward-model" scheme could also be used here:

$$\Phi\left(r_e\right) = \frac{1}{4\pi\sigma}\sum_{n=1}^{N}\frac{I_n}{\left|r_e - r_n\right|} \tag{3.1}$$

where r_e is the distance away from the electrode and σ is the conductivity of the medium. After introducing CSD into this equation,

$$C\left(\overrightarrow{r_e}\right) = \sum_{n} I_n\left(\overrightarrow{r_e} - \overrightarrow{r_n}\right) \tag{3.2}$$

it is natural to obtain the relation between the CSD and the potentials:

$$\Phi\left(\vec{r}\right) = \frac{1}{4\pi\sigma}\int d^3\overrightarrow{r'}\frac{C\left(\overrightarrow{r'}\right)}{\left|\overrightarrow{r'} - \vec{r}\right|} \tag{3.3}$$

After inverting this relation, it could obtain another Poisson equation:

$$C\left(\vec{r}\right) = -\sigma\Delta\Phi = -\nabla\cdot\left[\sigma\nabla\Phi\right] \tag{3.4}$$

Once the mathematic model of the relationship between the LFP and CSD is exposed, it is possible to compute the CSD from the LFP directly by numerical methods. The simplest numerical approximation is second-order finite differences:

$$\begin{cases} CSD(x) = [LFP(x+dx) - 2LFP(x) + LFP(x-dx)]/dx^2 \\ CSD(y) = [LFP(y+dy) - 2LFP(y) + LFP(y-dy)]/dy^2 \\ CSD(z) = [LFP(z+dz) - 2LFP(z) + LFP(z-dz)]/dz^2 \end{cases} \tag{3.5}$$

This approximation method was first introduced by Pitts in 1952 and much work has been devoted into it in the past decades [24–26], which is usually referred as traditional CSD (tCSD) method. For a more accurate approximation, some advances are proposed by researchers. Among them, smoothing the measurements with a Hamming window which obtains a five-point formula in one dimension gained some popularity:

$$\begin{aligned} CSD(z) = [&0.23 * LFP(z-2dz) + 0.08 * LFP(z-dz) - 0.62 * LFP(z) \\ &+ 0.08 * LFP(z+dz) + 0.23 * LFP(z+2dz)]/dz^2 \end{aligned} \tag{3.6}$$

In the recent years, the generality of this approximation method has been questioned due to the unavoidable edge effect. To eliminate these unnecessary boundary effects, some improved CSD estimation methods have been proposed. In 2006, a new, model-based, approach to estimate CSD has been generated, which is called as inverse CSD (iCSD). Compared to the traditional CSD, iCSD allows more general assumptions for the geometrical distribution of the sources. Here, the generality means that this method could integrate any prior knowledge or arrangement about the net current sources, such as the lateral size of columnar activity or direction-dependence of the extracellular conductivity [24]. Furthermore, this method could estimate the CSD at the position near the boundary, which is especially important due to that the estimation is based on the three-dimensional configurations, where half of the electrodes in the array could be set near the boundary.

The idea behind iCSD is to establish the "forward-model" scheme first to describe the filed potentials of local currents, which is based on the prior knowledge or assumptions. Then

an inverse matrix will be employed to calculate the source from the experiments. For example, assuming there are positions $\vec{x}_1, \ldots, \vec{x}_N$ and their corresponding potentials $\Phi_1, \ldots, \Phi_N$. Then it takes the values of CSD at measurement points $C_1, \ldots, C_N$ as parameters used to calculate CSD,

$$C\left(\vec{x}\right) = \sum_{k=1}^{N} C_k f_k\left(\vec{x}\right) \tag{3.7}$$

where function $f_k\left(\vec{x}\right)$ is the impulse function at the position $\vec{x}_k$. From the Eq.(3.3), there could exist a matrix relationship between the measured potentials and net current sources as $\Phi_j = \sum_k M_{jk} C_k$, where

$$M_{jk} = \frac{1}{4\pi\sigma} \int d^3 \overrightarrow{x'} \frac{f_k\left(\overrightarrow{x'}\right)}{\left|\vec{x}_j - \overrightarrow{x'}\right|} \tag{3.8}$$

A relation matrix F consists of the elements M_{jk} which leads a formula $\vec{\Phi} = F\vec{C}$. At the meanwhile, inverting this formula could reveal C_k is also the function of measured potentials, $\vec{C} = F^{-1}\vec{\Phi}$. A convenient feature of iCSD method is that the inverse matrix F^{-1} could be set up as a prior knowledge of the sources. This flexible framework of iCSD could make it enhanced by combining with kernel techniques (kernel CSD, kCSD) [18] or single-cell analysis (spike CSD, sCSD) [19].

3.2 Independent Components Analysis

As an extension to the principal component analysis (PCA), independent component analysis (ICA) also has a long history of application on data and signals analysis. PCA is a method based on singular value decomposition (SVD), which uses the property of second-order statistics of the signals. Its aim is to eliminate correlation of each decomposed component, which is widely used in data compressing. On the other hand, ICA is a method based on the property of higher-order statistics of signals, which ensure that every component is independent of each other. Due to the features of independence, ICA is generally applied on the blind sources separation (BSS) problem, such as cocktail problem. Although ICA was proposed as an extension to PCA [27], there still exists some different explanations about the

common transform formula $y = W^T x$. For PCA, y is only the projection of the input data x on the direction with the largest variance in the input space. As for ICA, the subcomponents of y are required to be independent of each other. The columns of matrix W construct subspace of input data. And for PCA, these column vectors are orthogonal with each other, along the direction with the largest variance. However, in ICA, these column vectors are not orthogonal any more, along the most significant direction of the non-gaussian distribution. This difference leads to distinct property of PCA and ICA. In terms of mean square error, the advantage of PCA is approaching to the original data, which is behaves well in data compressing. But this expression does badly in reflecting the special property of the original data, which is better in ICA. Furthermore, this difference also affects the application of the algorithms. PCA only considers the second-order statistics, which is enough for gaussian distribution. But it still has limits on non-gaussian distribution due to the additional information behind the higher-order statistics. To represent the essential features of the input data, ICA utilizes its higher-order statistics property. Thus, PCA is a standard algorithm and ICA does not have fixed standard, which will have different results based on different objective functions.

3.2.1 Mathematical Analysis of ICA

The core idea of ICA is to decompose some statistically independent components from the observed data by the linear decomposition. In the earliest expression of Jutten and Herault [27], ICA was simply defined as the method to find the source signals from linear mixed signals. The starting point for ICA is the very simple assumptions that components must be statistically independent and the independent components must follow the non-gaussian distribution.

Assume n linear mixtures of n independent sources are observed,

$$x_j = a_{j1} s_1 + \ldots + a_{jn} s_n \tag{3.9}$$

for all j. Written in matrix form, it will be

$$X = AS = \sum_{j=1}^{n} \vec{a}_j S_j \tag{3.10}$$

where, S is the matrix consist of independent sources $s_1, \ldots, s_n$ and X is the matrix made up of observed mixtures $x_1, \ldots, x_n$. At the meanwhile, the mixing matrix is denoted by matrix A with elements a_{ij}. The sources, so-called independent components, are invisible variables observed mixtures, as unknown as the mixing matrix. The aim of ICA is to estimate both mixing matrix A and independent sources S under as general assumptions as possible. To complete this estimation, the simplest trial is to calculate the inverse matrix of the mixing matrix. Assume there exists a separation matrix $W = A^{-1}$, , it could be available to separate the independent components through $S = WX$. Although this mathematical model is simple, it also leads to two main ambiguities of ICA: (1) The variances (energy) of the independent components could not be determined. (2) The order of independent components could not be determined as well.

3.2.2 Independence

Since the independence is the foundation of ICA, it is necessary to introduce the definition and fundamental properties of independence.

In probability theory, two events are independent, statistically independent, or stochastically independent if the occurrence of one does not affect the probability of occurrence of the other. Written in mathematics, it is defined by the probability density function (pdf). Introducing two random variables, y_1 and y_2 with the pdf $p(y_1)$ and $p(y_2)$. If these two random variables are independent, the joint pdf of them must satisfies the following way,

$$p(y_1, y_2) = p(y_1)p(y_2) \tag{3.11}$$

The definition could be easily used to derive another most important property of independent random variables,

$$E[y_1, y_2] = E[y_1]E[y_2] \tag{3.12}$$

which also indicates two random variables are uncorrelated.

This uncorrelatedness is a weak form of independence, which could be derived from the property of independence, but it is impossible to come to the conclusion that two variables

are independent of each other from uncorrelatedness. Since independence implies uncorrelatedness, many ICA methods give back uncorrelated estimates of the independent components by constraining the estimation procedure, which will reduce the free parameters for simplifying the problem.

As mentioned in the above, one of the starting points of ICA is non-gaussian distributed input data. This demand is risen form the nature of gaussian distribution. Assuming two gaussian distributed random variables, x_1 and x_2, and their joint pdf is

$$p(x_1, x_2) = \frac{1}{2\pi} \exp\left(-\frac{x_1^2 + x_2^2}{2}\right) \tag{3.13}$$

In the Figure 4, the distribution is illustrated that the density is thoroughly symmetric, containing no information useful on the directions of the column vectors in the mixing matrix. Thus, the mixing matrix A could not be estimated.

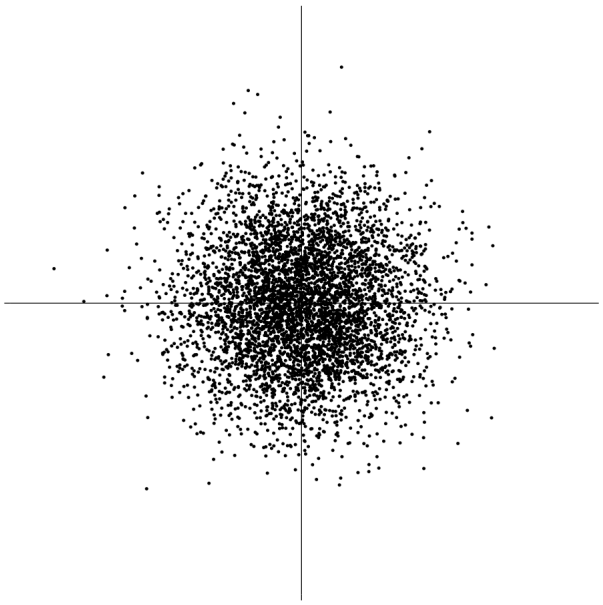

Figure 4: The Multivariate Distribution of Two independent Gaussian Variables

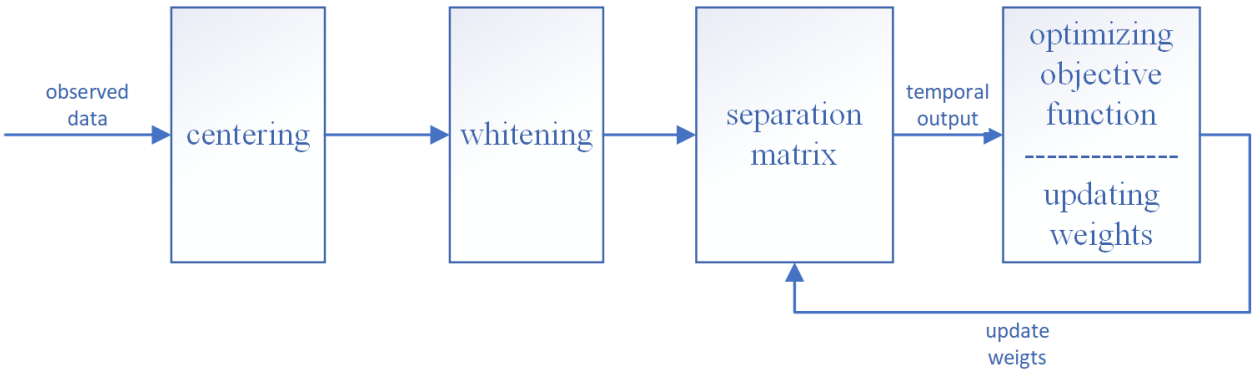

Figure 5: The Flow Chart of ICA

3.2.3 The Procedure of ICA

The application of ICA algorithm is usually divided into three parts: (1) whitening the input data (2) going through the separation matrix (3) optimizing the objective function and update the weights of separation matrix, just as the flow chart in the Figure 5. Firstly, the whitening procedure of input data could be applied by PCA, which has an obvious advantage that it performs well when the number of sources is far less than the number of the dimension of input data. Using M to denote the number of sources and L to denote the number of dimension, the largest M eigenvalues, $\lambda_1, \ldots, \lambda_M$, of the covariance matrix of input data represents the linear combination of the power of sources and noise. And the rest $L - M$ eigenvalues only correspond to the noise. Thus, whitening input data could compress data and eliminate noise as well, which usually makes the estimation algorithm converge more quickly and more robustly. However, whitening input data could also make the estimation harder when some sources are too weaker than the others. For the cases where input data is too much, PCA neural network could be employed to improve the performance.

3.2.4 Estimation Algorithm of ICA

There are many approaches of estimation for ICA, such as maximization of nongaussianity, minimization of mutual information, infomax and maximum likelihood estimation.

Although each approach is from different ideas, they could all be attributed to the extension to maximum likelihood estimation. At the meanwhile, the employment of these approaches is also divided into two methods: (1) batch (offline method) (2) stochastic gradient descent (online method). The batch method is widely used in the situation requiring no real time data processing with a much faster speed of convergence. By contrast, the stochastic gradient descent method usually employs neural network with ability of self-adjusting, which could deal with input data in real time. But it also leads to a slow speed of convergence and a strong dependence on the length of steps.

3.2.4.1 Maximization of nongaussianity Since the prior knowledge of ICA is lacked in the most cases, the mathematical basis for ICA to separate sources is central limit theorem, which tells that when independent random variables are added, their properly normalized sum tends toward a normal distribution even if the original variables themselves are not normally distributed. Therefore, it is possible to identify the independent components by measuring the nongaussianity of each subcomponent of output data. Generally, two kinds of measurement of nongaussianity are widely used in ICA, kurtosis and negentropy.

The classical measurement of nongaussianity is kurtosis or the fourth-order cumulant. For a random variable , the kurtosis is defined by

$$kurt(y) = E\left[y^4\right] - 3\left(E\left[y^2\right]\right)^2 \tag{3.14}$$

Since the input data has been preprocessed by centering and whitening, it could be of unit variance. Thus, the definition could be simplified as

$$kurt(y) = E\left[y^4\right] - 3 \tag{3.15}$$

For a gaussian variable, kurtosis is zero. And kurtosis is nonzero for most non-gaussian random variables. If the kurtosis of a random variable is positive, the random variable could be called super-gaussian. By contrast, the random variable with negative kurtosis is called sub-gaussian.

A second very important measurement of nongaussianity is given by negentropy, which is based on the concept of entropy in information theory. In the field of information theory,

the entropy is interpreted as the measurement of uncertainty of information, which means the more random a variable is, the larger its entropy is. The entropy H for a discrete random variable Y is defined by

$$H(Y) = -\sum_i P(Y = a_i) \log \left(P(Y = a_i) \right) \tag{3.16}$$

where a_i is the possible value of Y. For a continuous-valued random variable y, the formula could be expanded to

$$H(y) = -\int f(y) \log \left(f(y) \right) dy \tag{3.17}$$

where $f(y)$ is the probability density function of random variable y. To relate the entropy with the negentropy, one fundamental principle should be introduced that a gaussian variable has the largest entropy among all random variables of equal variance. This theory gives the entropy the ability to measure the nongaussianity. Since the gaussian distribution is the most random and the least structured, with largest entropy, the discrepancy between the entropy of other distribution and the entropy of gaussian distribution could indicate the nongaussianity. This discrepancy is called by negentropy

$$J(y) = H(y_{gauss}) - H(y) \tag{3.18}$$

where y_{gauss} is a gaussian random variable which has the same covariance matrix as y. As is known that gaussian random variable always has the largest entropy among the random variables with same covariance matrix, the negentropy should always be greater or equal to zero. It will be equal to zero only if the variable y is gaussian distributed.

Measuring nongaussianity by negentropy is in some sense the optimal estimator because it is justified by statistical theory. However, estimating negentropy using the definition require estimating the pdf of random variables firstly, which makes the calculation overly complex. Therefore, simpler approximation is introduced to help estimate negentropy

$$J(y) \approx \frac{1}{12} E\left[y^3\right]^2 + \frac{1}{48} kurt(y)^2 \tag{3.19}$$

3.2.4.2 Minimization of Mutual Information Another approach for ICA estimation inspired by information theory is minimization of mutual information. Similar as nongaussianity measurement, mutual information is used to find the most non-gaussian directions as well.

Before introducing mutual information, the definition of Kullback-Leibler divergence should be imported in advance. Assuming the pdf of random variables w and z is $w(x)$ and $z(x)$, the Kullback-Leibler divergence of these random variables is defined as

$$K\left(w|z\right) = \int w(x) \log[w(x)/z(x)]dx \tag{3.20}$$

This integration will be valid and non-negative consistently, and it will be equal to zero if and only if these two random variables are following the same distribution. Obviously, Kullback-Leibler divergence could measure how much the difference between the distributions of these two random variables is in quantity, which could be considered as the "distance" between the two kinds of distribution.

Assume a multi-dimension random vectors $\vec{y}$ is made up of scalar random variables $y_1, \ldots, y_M$, the mutual information I between these random variables is defined by the Kullback-Leibler divergence of the joint probability distribution density of $\vec{y}$ multiplying the marginal density of y_i,

$$\begin{aligned} I\left(y_1, \ldots, y_M\right) &= K\left[p(\vec{y})|\prod_i p_i(y_i)\right] \\ &= \int p(\vec{y}) \log\left[p(\vec{y})|\prod_i p_i(y_i)\right] \\ &= \sum_i \int p_i(y_i) \log\left(p_i(y_i)\right) - \int p(\vec{y}) \log\left(p(\vec{y})\right) d\vec{y} \\ &= \sum_i H(y_i) - H(\vec{y}) \end{aligned} \tag{3.21}$$

This mutual information $I\left(\vec{y}\right)$ is measuring the independence of each subcomponent of random vectors $\vec{y}$. It is always non-negative and will be zeros once the subcomponents are statistically independent. Therefore, minimizing the mutual information could lead to decomposing independent component for ICA.

Additionally, for those ICA algorithms employing the neural network, the weights matrix could be updated by the following equation,

$$W_{k+1} = W_k + \mu \left(I - f(y) y^T \right) W_k \tag{3.22}$$

where $f(y)$ is an odd function or a monotonic transfer function.

3.2.4.3 Infomax Method As mentioned in the above, $y = WX$, W is the separation matrix and X is the observed data. Then there exists a nonlinear transfer function f on output data y, which follows

$$z = f(y) = f(WX) \tag{3.23}$$

where z is the transformed signals. Certainly, the transformed signals z has its own entropy

$$H(z) = -\int p(z) \log(p(z)) dz \tag{3.24}$$

If the transfer function is differentiable and satisfy the constrains,

$$\int_{-\infty}^{\infty} f_i'(y_i) dy_i = 1 \tag{3.25}$$

the entropy of z will be maximized, and y_i is the subcomponent desired. In fact, when $f_i(x)$ is the distribution function of the real independent signal sources s_i, maximizing the entropy of z is equivalent to minimizing the mutual information of y.

3.2.4.4 Maximum Likelihood Estimation Another popular approach for the ICA is maximum likelihood estimation. Given the observed data X, the separation matrix W, and the independent sources S, $S = WX$, the joint probability density function of S,

$$f(S) = \prod_i f_i(s_i) \tag{3.26}$$

and the pdf of X,

$$p(X) = |\det(W)|\, f(WX) \tag{3.27}$$

have the negative likelihood function

$$\begin{aligned} G(W) &= -\sum_j^n \log(p(x_j)) \\ &= -n \log\left(|\det(W)|\right) - \sum_j^n \sum_i \log(f_i(S_i)) \end{aligned} \tag{3.28}$$

The globally minimum solution W is the separation matrix desired for ICA. This W could be approached by

$$W := W - \eta \left(E\left[\Phi(S)S^T\right] - I\right) W \tag{3.29}$$

where η is the learning rate and E is the expecting operator, I is the unit matrix, and

$$\Phi(S) = \left[\varphi_1(s_1), \cdots, \varphi_M(S_M)\right]^T \tag{3.30}$$

where

$$\varphi_j(S_j) = -\left[\log\left(f(s_j)\right)\right]' = -f'(s_j)/f(s_j) \tag{3.31}$$

3.3 FastICA

Most popular ICA algorithms are based on the nongaussianity estimation approaches mentioned above. In this section, we introduce the widely used fixed-point fastICA algorithm, which is based on the negentropy estimation. Here, it is assumed that the data is preprocessed by centering and whitening.

As explained in the previous section, it is difficult to calculate negentropy from the definition directly. To simplify the calculation procedure, higher moment is used:

$$J(y) \propto \left[E\left\{G(y)\right\} - E\left\{G(y_{gauss})\right\}\right]^2, \tag{3.32}$$

where $G(y)$ is a higher moment of y. The core of fixed-point fastICA algorithm based on negentropy is an iteration approach used to find the fixed-point with maximum nongaussianity. Before the iteration, a nonlinear function g should be determined, which is commonly the derivative of the non-quadratic function G used in the measurement of negentropy. To ensure the robustness of the results, G might have a weak response to the increasement of independent variable. The following are the functions widely used

$$\begin{cases} G_1(u) = \log(\cosh(u)) \\ G_2(u) = -\exp(-u^2/2) \\ G_3(u) = u^4 \end{cases} \tag{3.33}$$

Assume input data is Z and its weights vector is W, the variance of $W^T Z$ must be unitized, which is equivalent to that the norm of W is also unitized for whitened input data Z. When the iteration begins, the initial iteration is

$$(1+a)W = E\left\{Zg\left(W^T Z\right)\right\} + aW \tag{3.34}$$

After each iteration, weights vector should be normalized. The maximum negentropy of $W^T Z$ will be found at the extreme point of $E\left\{G\left(W^T Z\right)\right\}$, under the constrains

$$\left\{\left(W^T Z\right)^2\right\} = W^2 = 1 \tag{3.35}$$

Considering that input data has been whitened, the updating could be solved by Quasi-Newton Method

$$W \leftarrow W - \left[E\left\{Zg\left(W^TZ\right)\right\} + \beta W\right] / \left[E\left\{g'\left(W^TZ\right)\right\} + \beta\right] \tag{3.36}$$

After simplification, the updating could be written as

$$W \leftarrow E\left\{Zg\left(W^TZ\right)\right\} - E\left\{g\prime\left(W^TZ\right)\right\} W \tag{3.37}$$

Therefore, the procedure of iteration is interpreted as the following (Also, see Figure 6):

(1) Choose a random weights vector W with unitized norm.

(2) First iteration of updating: $(1+a)W = E\left\{Zg\left(W^TZ\right)\right\} + aW$, then normalize W.

(3) Update W: $W \leftarrow E\left\{Zg\left(W^TZ\right)\right\} - E\left\{g\prime\left(W^TZ\right)\right\} W$, then normalize W.

(4) If the weights vector does not converge, return to step 3; If the weights vector does converge, then finish the iteration.

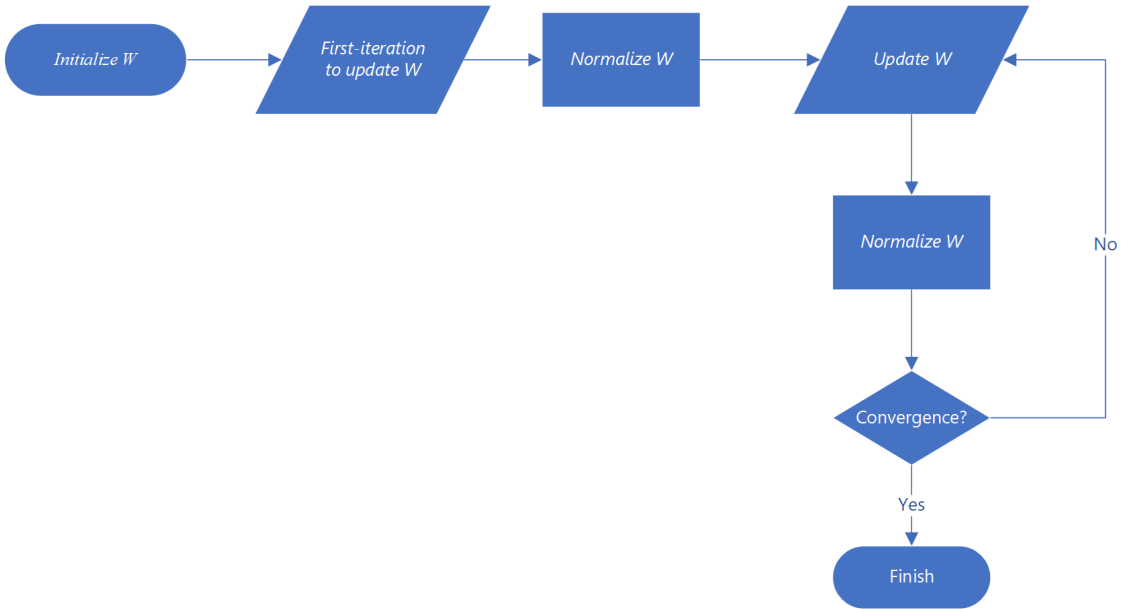

Figure 6: The Flowchart of Updating Weights

3.4 Source Clustering Algorithm

Aiming to pinpoint the independent components which could capture of the characteristics of source generators consistently, we cluster the resultant ICs from different bootstaps. The clustering method uses a combination of independent components to be found on each bootstrap instead of using an initial run. The benefits of these repeated trials are that ICA has more chance to approach the optimal solution under various initial conditions, especially for some special situations. Here, for a smaller computation consumption, bootstrapping is employed in each trial. After multiple runs, the mixing matrix A in each run of ICA is concatenated into

$$A^{all} = \left[A^1, A2, \ldots, A^N\right] \tag{3.38}$$

where A^n is the mixing matrix in run n and N is the number of total runs.

Before clustering the column vectors of the combined mixing matrix A^{all}, normalizing the columns in the matrix will to get rid of the scale ambiguities of ICA and reduce the consumption in computing as well.

$$\hat{a}_i = \frac{a_i - \bar{a}_i}{\|a_i - \bar{a}_i\|} \tag{3.39}$$

where a_i is the column vector in the combined mixing matrix and $\bar{a}_i$ is the mean of a_i. The original concatenated matrix A_{all} is turned to a normalized form $\hat{A}$. To measure the similarities of this normalized results, the best way is using correlation. The correlation matrix C is made up by

$$c_{ij} = corr\left(\hat{a}_i, \hat{a}_j\right) \tag{3.40}$$

Aiming to find consistency, which means only those significant similarities will be appealed, the binarization could be employed to simplify the correlation matrix C

$$\bar{c}_{ij} = \begin{cases} 1 & \text{if} |c_{ij}| > \varepsilon \\ 0 & \text{if} |c_{ij}| < \varepsilon \end{cases} \tag{3.41}$$

where ε is the threshold used for binarization and $\bar{C}$ is the finally binary matrix.

Furthermore, two column vectors might not be related to each other directly, but they could be related through a long path, where $\hat{a}_i$ is related to $\hat{a}_j$ and $\hat{a}_j$ is related to $\hat{a}_k$. To overcome this long path ambiguities, the binary correlation matrix could be raised to suitable power,

$$R = \bar{C}^p \tag{3.42}$$

where p is the longest path acceptable.

Since the exact number of useful independent components is not known in prior, the traditional clustering methods like k-means could not be implemented here. Instead, it comes up with a simpler clustering algorithm, using correlation as the distance measurement without introducing other parameters. This algorithm works in two phases:

1. All related elements, which have a value r_{ij} equal to 1, are sorted in descending order by their corresponding absolute correlation value $|c_{ij}|$. Thus, the resulting list will hold the links between all component pairs in their order of importance.

2. Then, the clusters are formed by going through the following rules in order until each component a is attributed to a cluster.

   (a) If neither of the linked components $\hat{a}_i$ and $\hat{a}_j$ belongs to an existed cluster, then create a new cluster containing both of them.

   (b) If one of the linked components, $\hat{a}_i$ or $\hat{a}_j$, belongs to an existed cluster, then another one will be attributed to this cluster as well.

   (c) If both of the linked components, $\hat{a}_i$ and $\hat{a}_j$, belong to an existed cluster, skip them.

Once the clusters are determined, the components in the same clusters should be justified to a uniform sign and an average component should be computed from the components in the cluster. The same operation will be employed on their corresponding independent components as well. This procedure will be repeated until no more combination.

4.0 Neurophysiological Analysis

In this chapter, the results of neurophysiological analysis will be discussed and we try to discover the regulation of the procedure under covered.

4.1 Preprocessing data

Although the data recorded has passed through the filters, it is necessary to perform some preprocessing tasks before analysis as well. The most important three steps of the preprocessing procedure are: isolating desired channels, filtering, realigning and down sampling. First of all, since not all channels are useful in the analysis, too deep, too superficial and too noisy, isolating desired channels from the raw data should be considered as the fundamental step of preprocessing. After excluding useless channels, going through the high-pass filter at 1 Hz could be helpful to filter the DC signals. Next step is to realign the target parts of the signals and saccade parts of the signals from the original data. Shown in the Figure 7, around the time of target onset and the time of performing saccade task, we split two time-blocks both around 400ms separately. Then the realigned data is down sampled to the one quarter, every sampling points represent 4 milliseconds.

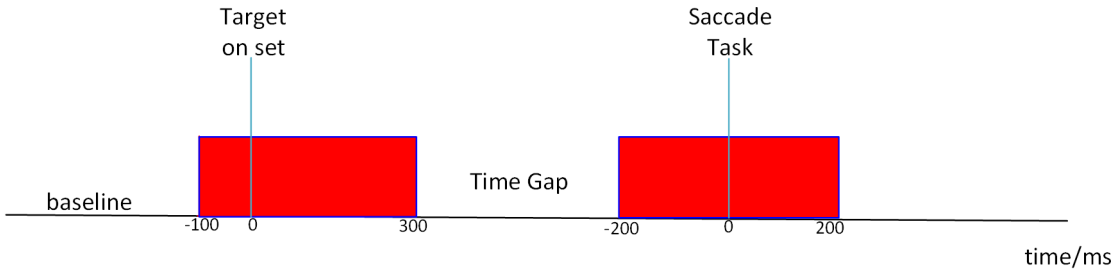

Figure 7: Time Blocks on Timeline

4.2 Results and Discussions

Finally, two ideal time blocks are extracted from the raw data, which will be used in the following analysis. To locate the source generators using ICA, two different kinds of hypothesis are proposed. One is to combine two blocks as a whole block to see whether the independent components could pick up the source generators desired in a global time scale, and another hypothesis is to divide the original blocks into smaller blocks to study the activities of source generators in a local time scale.

4.2.1 Simulation data

Before analyzing the real datasets, employing ICA on the simulation data could tell how the independent components and their corresponding mixing matrix reflect the temporal and spatial property of the source generators.

As mentioned in the above chapters, the LFPs are generated by transmembrane currents, which give rise to extra cellular electric fields and their corresponding electric potentials. From Eq.(2.4), it indicates that the electrical potentials V and volume current density C are related through a Poisson equation and could be written in the following format in three-dimension space:

$$V(x,y,z) = \frac{1}{4\pi\sigma} \int\int\int \frac{C\left(x',y',z'\right) dx'dy'dz'}{\sqrt{\left(x-x'\right)^2 + \left(y-y'\right)^2 + \left(z-z'\right)^2}} \tag{4.1}$$

where σ is the conductivity tensor.

And your model is transformed from three-dimensional space into a spatial-temporal plane, the formula is also transformed into:

$$V(x,t) = \frac{1}{4\pi\sigma} \int\int \frac{C\left(x',t'\right) dx'dt'}{\sqrt{\left(x-x'\right)^2 + \left(t-t'\right)^2}} \tag{4.2}$$

where the current source generators C is distributed as follows:

$$C(x,t) = C_V(x)C_t(t) \tag{4.3}$$

In this formula,

$$C_t(t) = e^{i2\pi ft} \tag{4.4}$$

and

$$C_V(x) = Ae^{-(x-L_1)^2/2\sigma_V^2} - (1-\varepsilon)Ae^{-(x-L_2)^2/2\sigma_V^2} \tag{4.5}$$

Here, A and $(1-\varepsilon)A$ are A are the amplitudes with opposite signs when $0 \leq \varepsilon \leq 1$. L_1 and L_2 are both inter-laminar locations and σ is the common width in vertical.

Here is the instances of simulation with different parameters in Figure 8.

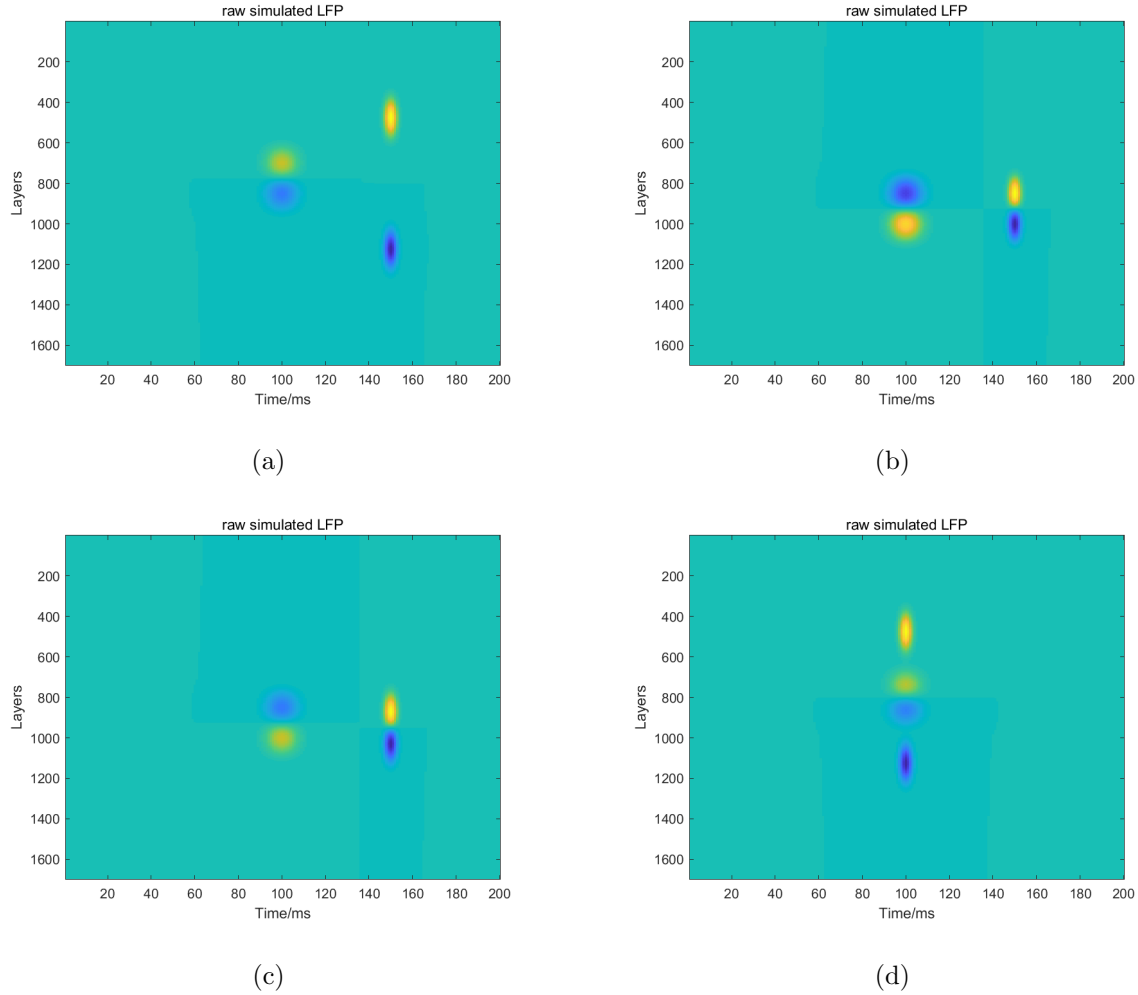

Figure 8: Four Different Simulation Datasets

From Figure 9(c), Figure 9(d) and Figure 9(e), it is noticeable to see that independent components will detect a sharp or flat peak when the generators burst. At the meanwhile,

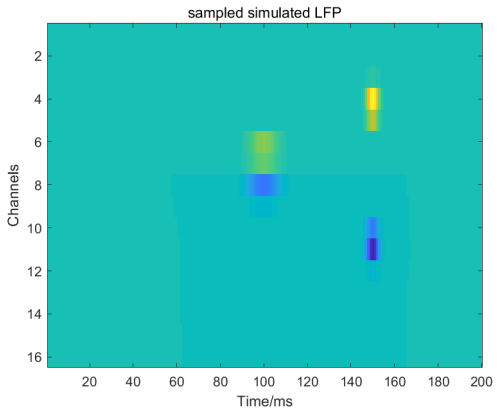

(a)

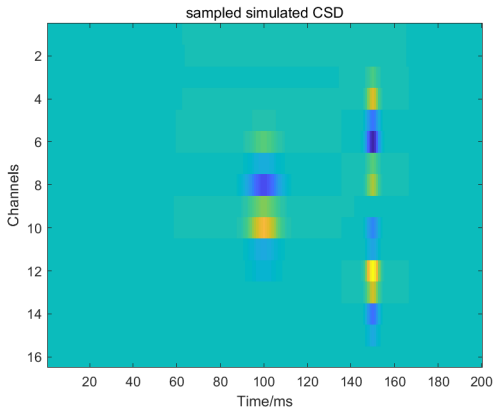

(b)

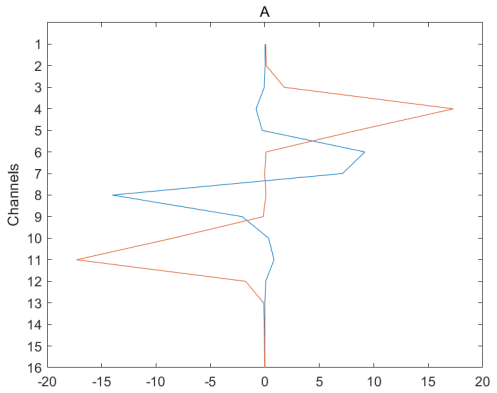

(c)

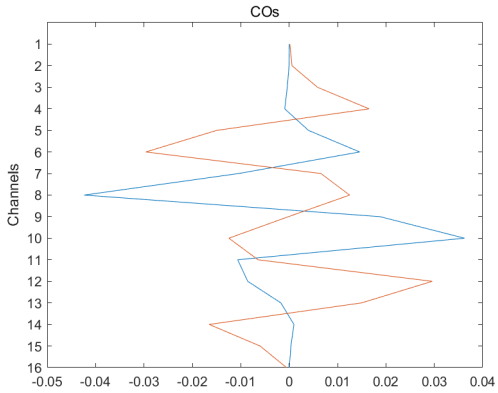

(d)

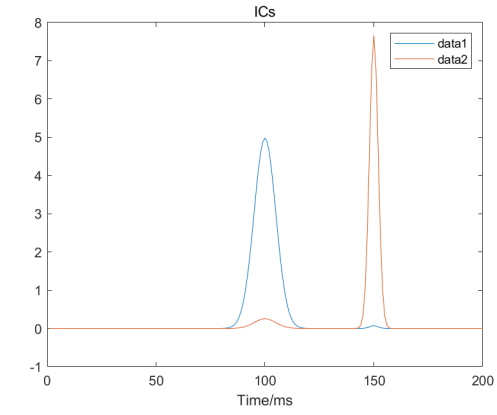

(e)

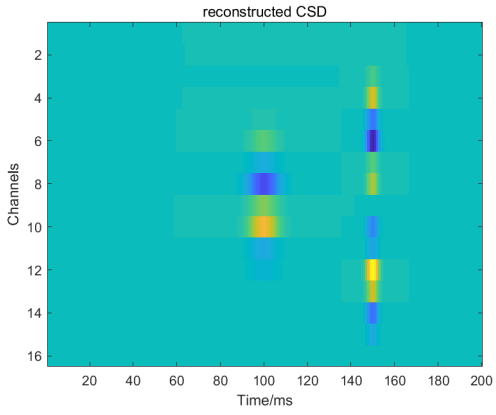

(f)

Figure 9: (a) LFP of Sampled Simulated Data (b) CSD of Sampled Simulated Data (c) Mixing Columns (d) 2^{nd} Derivative of Mixing Columns (e) Independent Components (f) Reconstructed CSD

when we plot the corresponding columns in the mixing matrix, there exist the protruding corners at the channels containing prominent potentials in the LFP figure. Applying second derivative on the columns of mixing coefficients, the resulted coefficients columns are called second derivative coefficients, whose corners are corresponding to the channels where the generators locate. Once multiplying the independent components by second derivative coefficients, it could be possible to reproduce a source generators location figure highly similar as the CSD figure. All following analysis is based on this assumption.

To verify the assumption and consider some special cases, ICA is applied on another three sets of simulation data. The results of these datasets show the consistent phenomenon and provide some special cases as well.

In Figure 10, it is apparent that two pairs of generators appear at the same layer with little difference at different points of the timeline. In this case, ICA picks up these two pairs of generators by only one independent components. At the meanwhile, in the Figure 11, two different pairs of generators are distributed at the same point as in Figure 10, but ICA catches two different independent components in this case, which could be considered the collateral evidence that ICA owns the ability to identify the different pairs of generators even if they burst at the same channel. In Figure 12, it introduces a special example which could explain some unexpected distortion of the independent components. In this instance, two pairs of generators burst in different channels at the same time point. It is apparent that one of the two peaks are suppressed by another peak. It implies that if several peaks burst at the same time, ICA could only identify one of them, and other peaks are all inhibited by this chosen one.

To verify the high similarity between the original CSD signals and reconstructed signals, we use correlation in two dimensional space to measure it. The results shown in the Table 1 indicates the original and reconstructed signals are highly similar as each other.

After employing ICA on those simulated datasets, the relationship between the number of independent components, the peaks of independent components and the protruding corners of mixing columns has been discovered and those properties are considered as reference while analyzing real data collected.

Table 1: Similarity between Original and Reconstructed CSD on Simulation Data Sets

Similarity between Original and Reconstructed CSD	
Set 1	0.9431
Set 2	0.9332
Set 3	0.9423
Set 4	0.9517

4.2.2 Global Time Scale

In this section and the following section, one dataset, BL071717, will be used as the instance, we will analyze this dataset from the scale in global and in local separately. Then, the outcome of analysis on other datasets will be provided in the following section as supplemental evidence for our assumption.

In Figure 13, it plots the figure of LFP and its corresponding CSD analysis. Once employing ICA on the LFP, as shown in the Figure 14, it is noticeable to catch several peaks in the target task plane and in the saccade task plane separately. The time coordinates of these peaks indicate when the source generators have a strong response to the task activity. Notice that in the procedure of target task, the response activates after a short delay, and in the procedure of saccade task, the response activates immediately. This property tells that there exists reaction time when monkeys see the target onset, and there is nearly no reaction time after performing saccade task. According to the figure, only a few independent components could pick up those peaks, which means those chosen independent components represent temporal property of those source generators. Performing ICA globally could not only give back the activity of the generators in temporal plane, but also tell the spatial information when the generators burst. However, these extracted independent components could not show the detailed response procedure of the generators. To study the detailed activity of generators during the procedure of the response under a tiny time scale, it is necessary to split the original time blocks to smaller epochs.

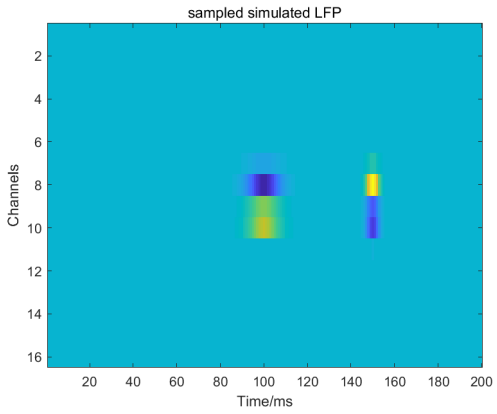

(a)

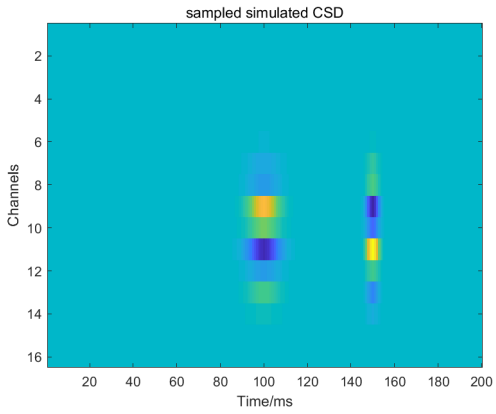

(b)

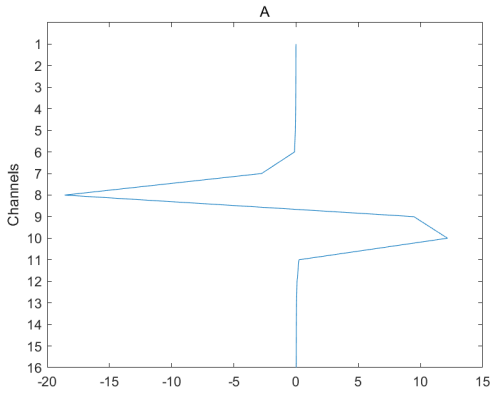

(c)

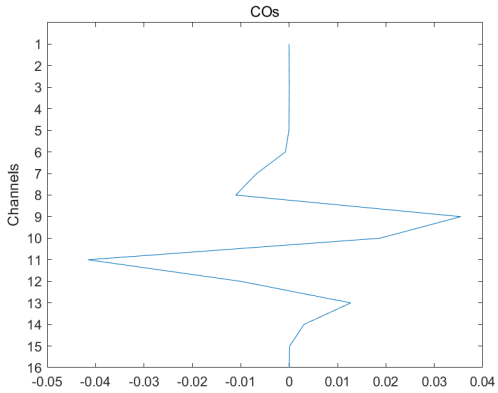

(d)

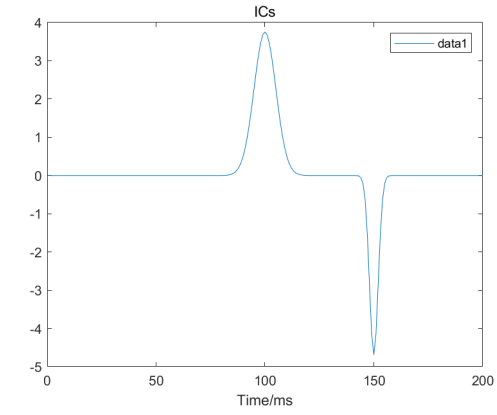

(e)

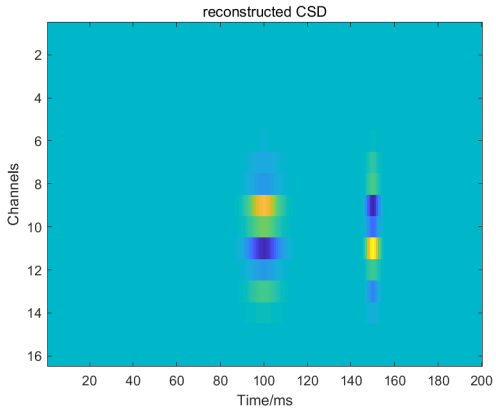

(f)

Figure 10: (a) LFP of Sampled Simulated Data (b) CSD of Sampled Simulated Data (c) Mixing Columns (d) 2^{nd} Derivative of Mixing Columns (e) Independent Components (f) Reconstructed CSD

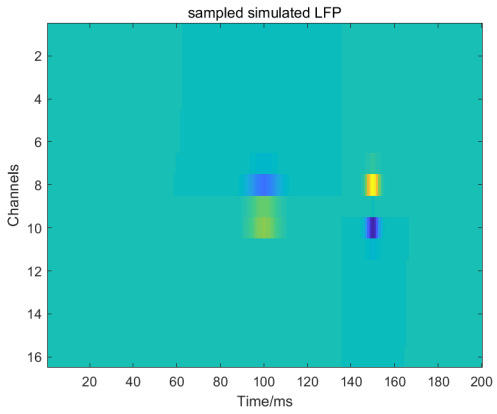

(a)

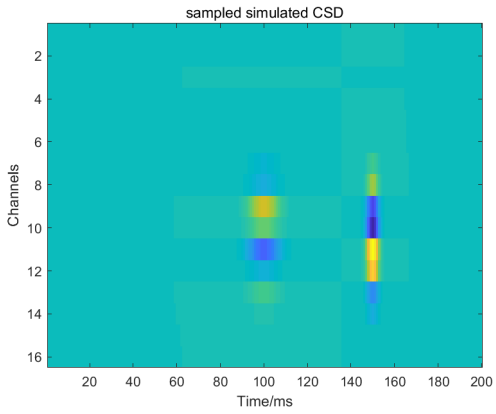

(b)

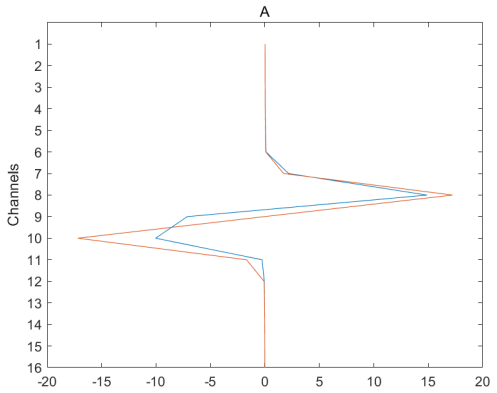

(c)

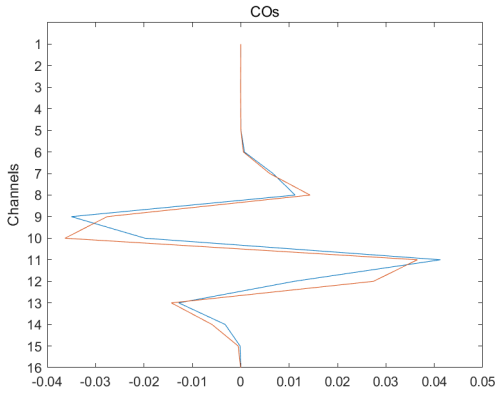

(d)

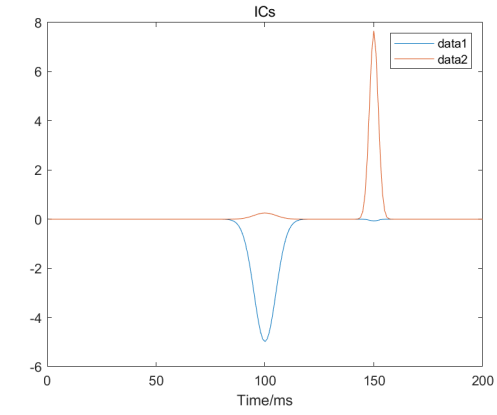

(e)

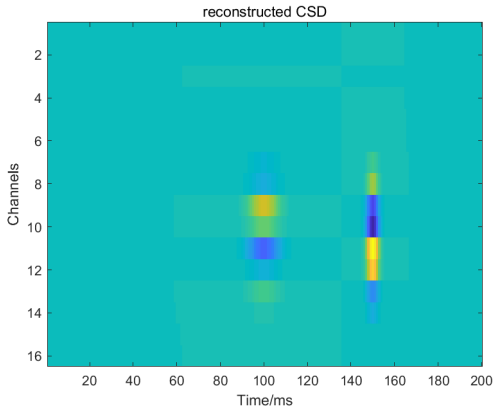

(f)

Figure 11: (a) LFP of Sampled Simulated Data (b) CSD of Sampled Simulated Data (c) Mixing Columns (d) 2^{nd} Derivative of Mixing Columns (e) Independent Components (f) Reconstructed CSD

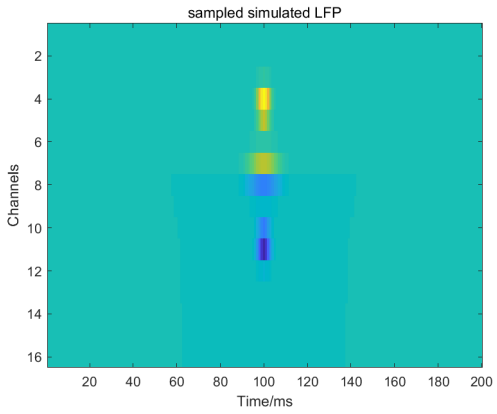

(a)

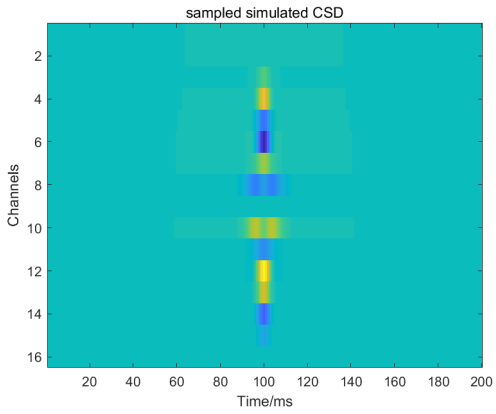

(b)

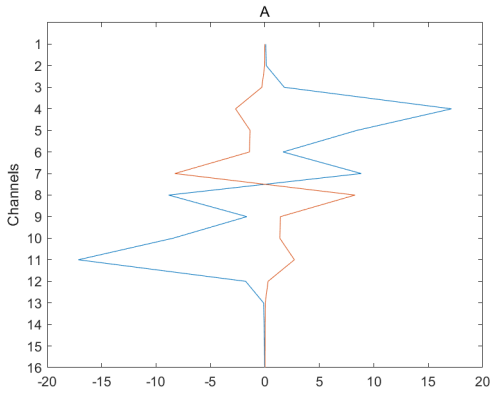

(c)

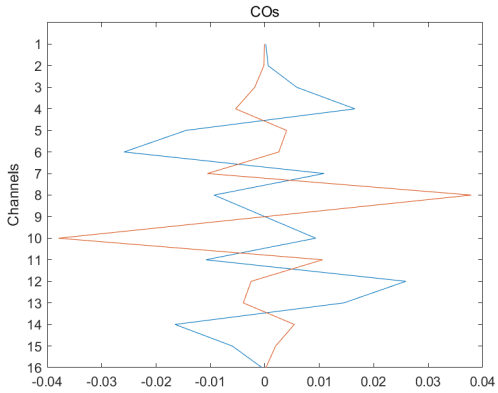

(d)

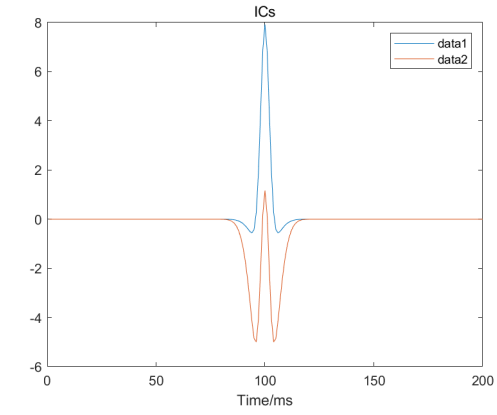

(e)

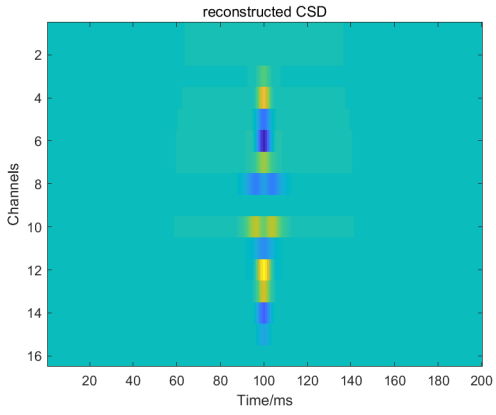

(f)

Figure 12: (a) LFP of Sampled Simulated Data (b) CSD of Sampled Simulated Data (c) Mixing Columns (d) 2^{nd} Derivative of Mixing Columns (e) Independent Components (f) Reconstructed CSD

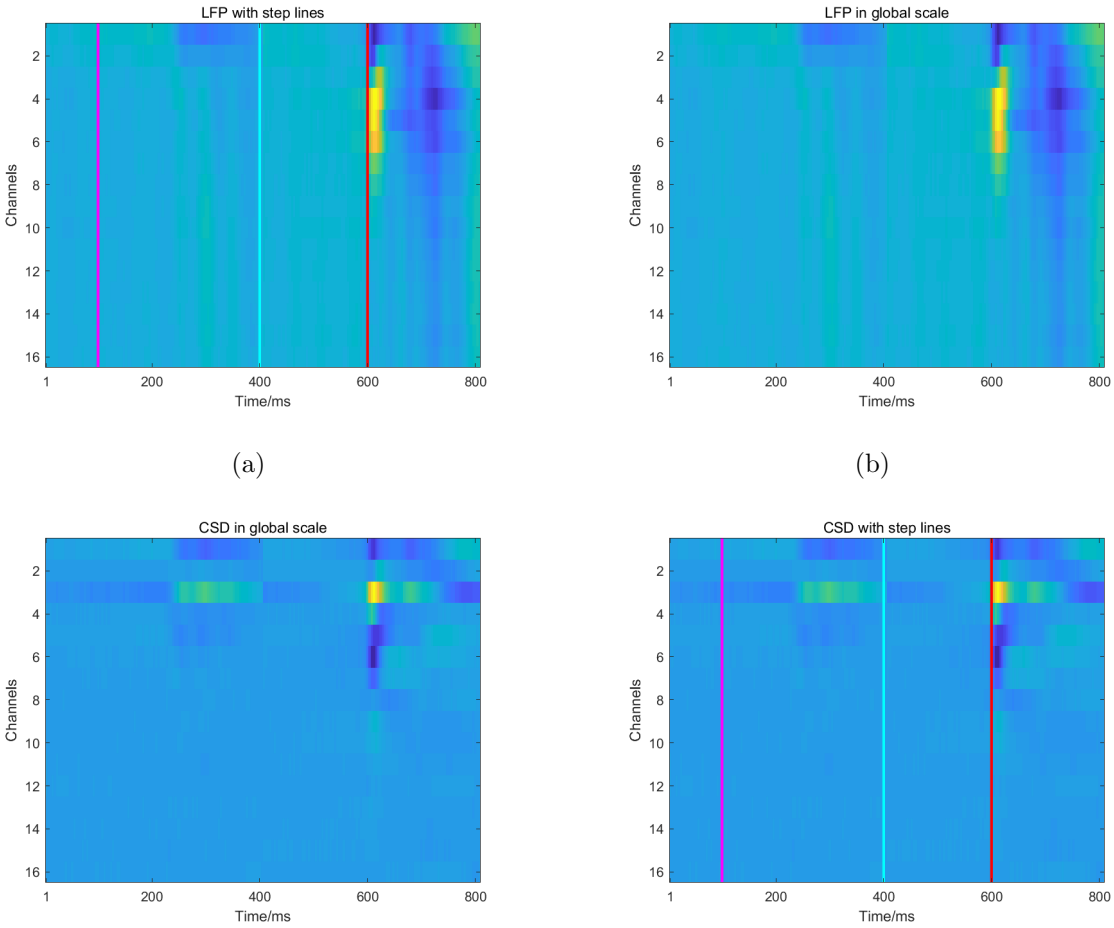

Figure 13: (a) LFP of Dataset (b) LFP of Dataset with Step Lines (C) CSD of Dataset (d) CSD of Dataset with Step Lines

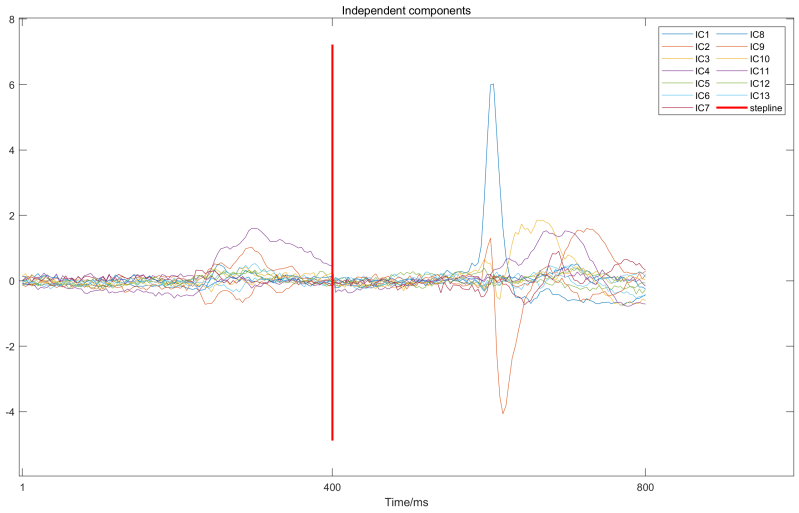

(a)

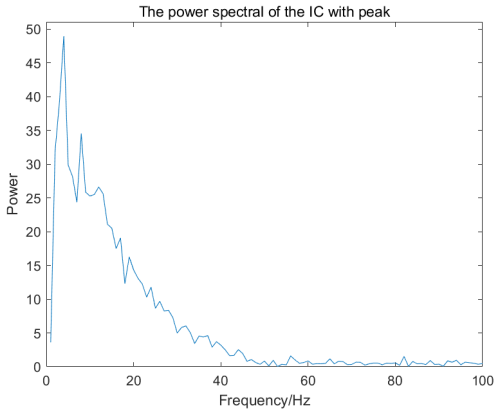

(b)

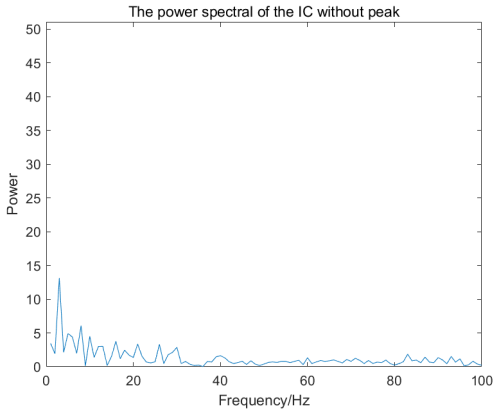

(c)

Figure 14: (a) Independent Components in Global Scale (b) Spectral Power of Peaking IC (c) Spectral Power of Residual IC

Despite of those independent components which carry abundant information by catching the peaks, the other independents appear to be noisy once they are transformed in the frequency plane. As shown in the Figure 14, the comparison between the components containing peaks and the components without peaks in frequency plane. In Fig.14(b), the spectra power centers at the low frequency area, and decays with the increase of the frequency. In Fig.Fig.14(c), it is apparent to find that the spectra power follows the uniform distribution in the frequency plane, which means the signals are gaussian white noise in common. The noise unfiltered in the preprocessing procedure is commonly considered as the background noise or the volume conduct activity from the adjacent regions. This result reflects another property of ICA, which could denoise the original data.

4.2.3 Local Time Scale

For an advanced research on the detailed activities of the generators during the procedure of performing the task, employing ICA on a smaller time epoch and analyzing the changes of those local source generators might return some extra information and help to discover some regular patterns of this target-saccade action.

According to the experiments in global time scale, it definitely has some limits on directly applying ICA on the epochs. Since the data recorded could not be pure enough without any noise affection, numerous independent components representing noise are extracted by ICA. To solve this problem, one clustering method has been proposed to help finding those consistent independent components carrying the information of generators in multiple trials.

Before clustering, it is necessary to define the time epoch, subcomponents of the blocks. For target task block, it is divided into four epochs: one hundred milliseconds before target onset; from the target onset to the one hundred milliseconds after that time; from the one hundred milliseconds after target onset to two hundred milliseconds after the activity; from target onset to two hundred milliseconds after the activity. At the meanwhile, the saccade task block is also divided into four epochs: one hundred before performing saccade task; from forty milliseconds before performing saccade task to sixty milliseconds after the activity; from performing saccade task to one hundred milliseconds after the activity; from one hundred

milliseconds after performing saccade task to two hundred milliseconds after the activity. Applying ICA separately on those epochs, the results sequence of those epochs will discover some templates behind the potentials varying.

In Figure 15-Figure 16, after comparing the time epochs divided from the CSD figures to the epochs from the reconstruction, second derivative coefficients multiplying independent components, it is clear that although there exists boundary effects on the reconstruction epochs in saccade task blocks, the reconstruction epochs provides a more clear figures locating the sources and sinks without the affection of noise from background and volume conduct activity. Furthermore, while focusing on the second derivative coefficients extracted from mixing columns which represents the spatial property of generators captured in the epoch, it could overcome the boundary effects and only concentrate on the action of generators in time sequence. In Figure 17-Figure 18, it is apparent that in channel 3 there exists a generator consistently during the whole procedure. However, the difference between the generator at channel 3 in target onset block and saccade task block is where its pairing generator locates. In target onset block, the pairing generator locates at top 2 channels, and in saccade task block, the pairing generator is transferring to channel 6 in the bottom. Once finishing the saccade task, the generators pairs recover the state as in target onset block, which also has a little similarity as pair distribution in the preparation state before target onset. The sequential epochs of second derivative coefficients in time sequence describes a procedure where generators move down and recovery with performing the target-saccade task. In the locally tiny epochs, it is safe to consider that the independent components represent the temporal property of the generators and the corresponding second derivative coefficients columns reflecting the spatial property as well.

And at the same time, the similarity measured by correlation between original and reconstructed CSD signals shows to be little lower than measurements on simulation data sets in local time epochs. This decrease could be explained by that the simulation data is generated under a noise-free condition and we exclude some independent components representing noise in clustering algorithm, which leads to the loss of some useless information. As shown in Table 2, the reconstructed CSD signals with all independent components has a high correlation with the original signals in global scale. We could safely consider this de-

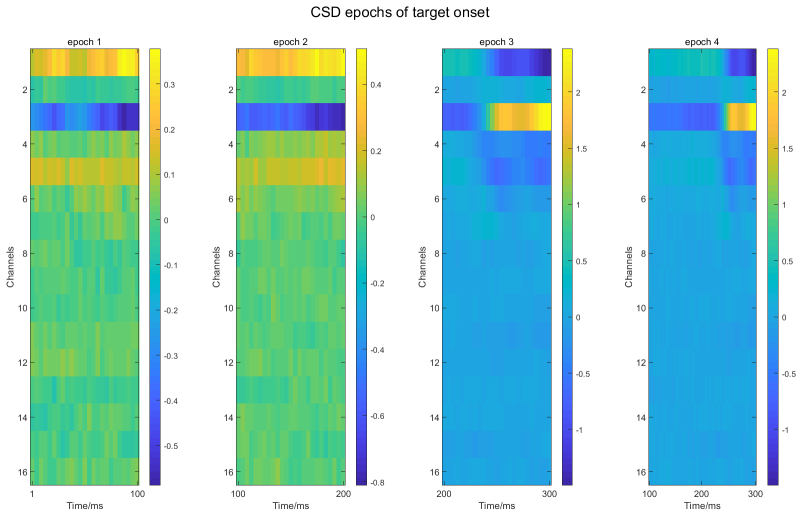

(a)

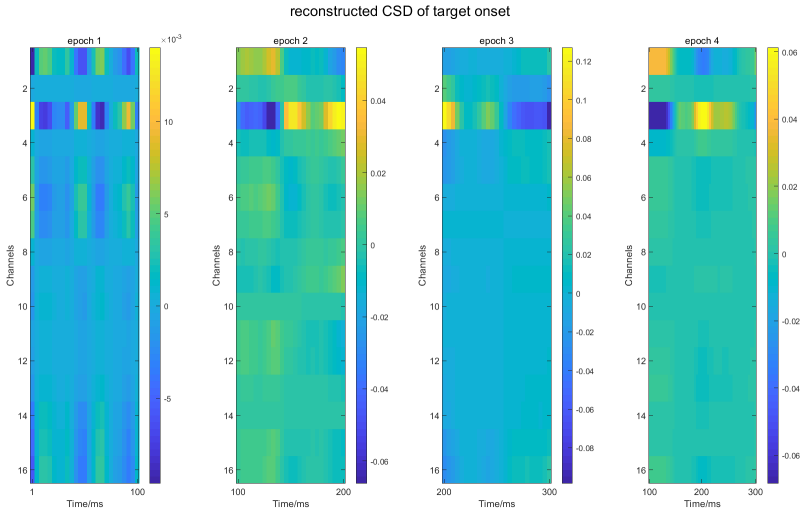

(b)

Figure 15: (a) CSD epochs of target onset block (b) reconstructed CSD epochs of target onset block

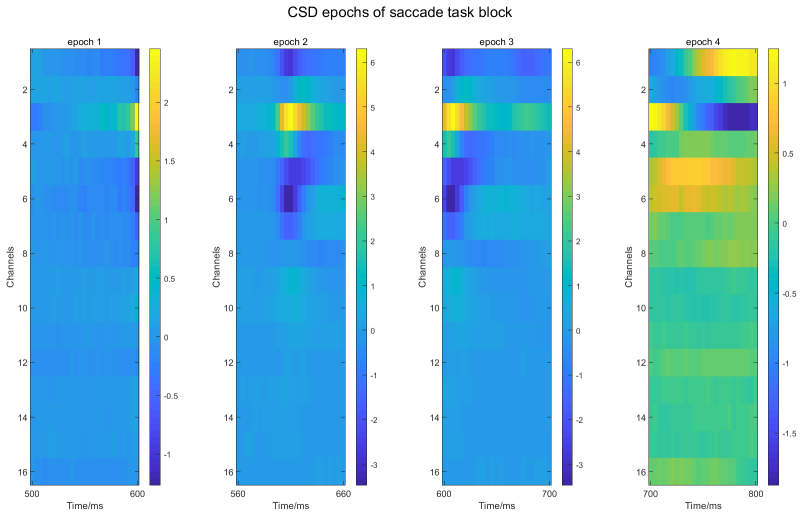

(a)

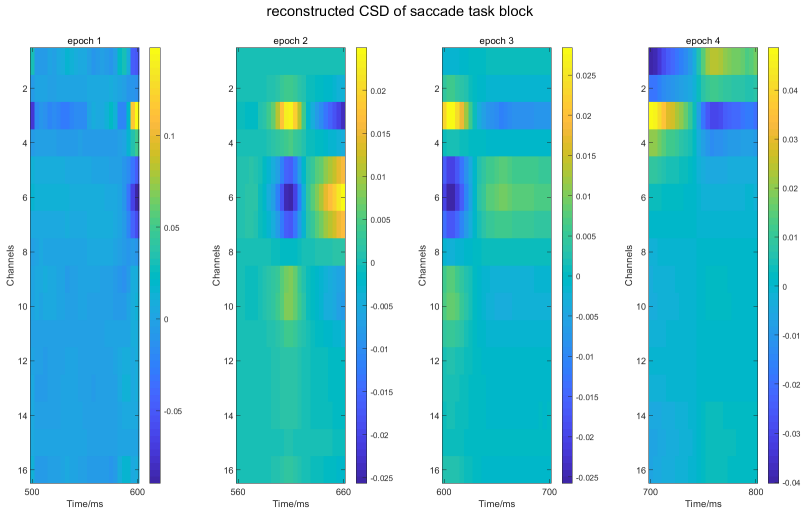

(b)

Figure 16: (a) CSD epochs of saccade task epochs (b) reconstructed CSD epochs of saccade task block

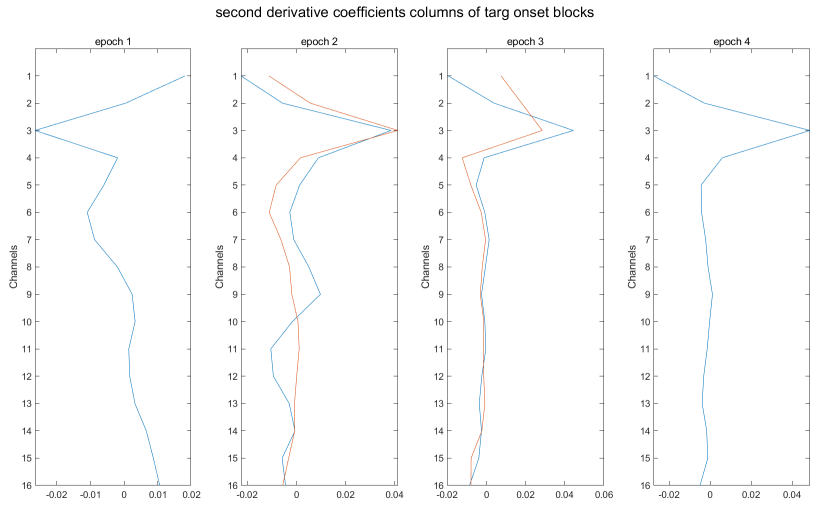

(a)

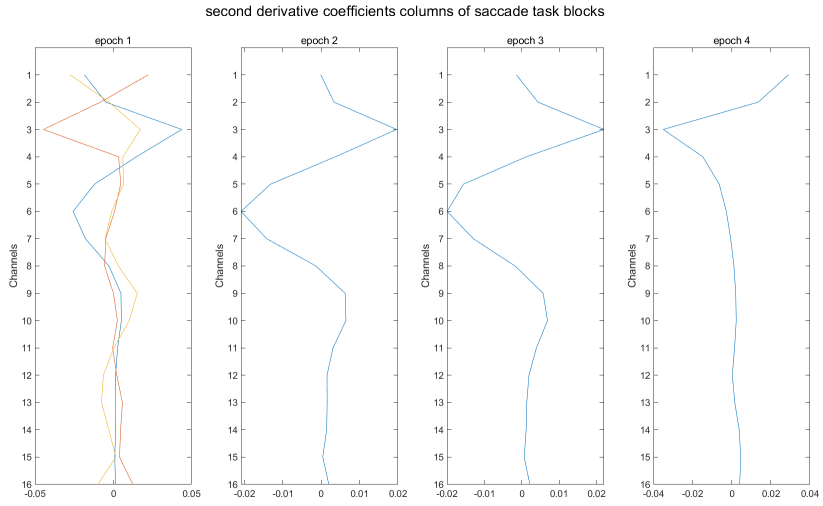

(b)

Figure 17: (a) 2^{nd} Derivative Coefficients of Epochs in Target Onset Block (b) 2^{nd} Derivative Coefficients of Epochs in Saccade Task Block

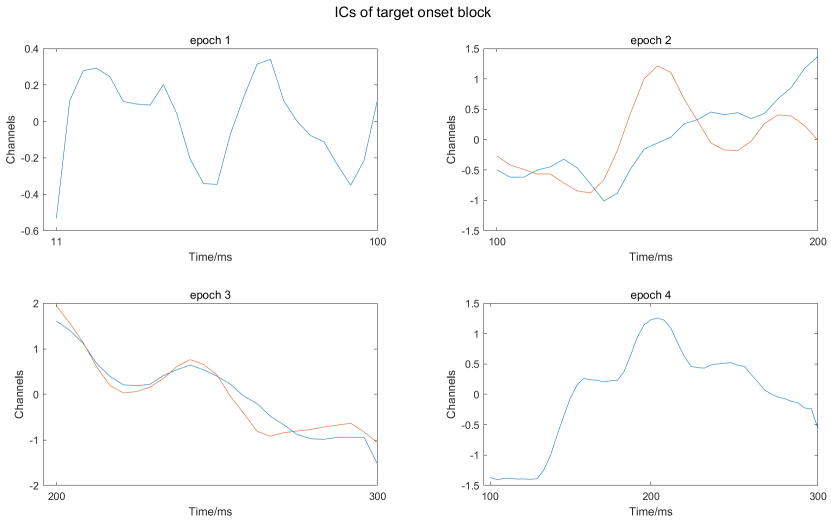

(a)

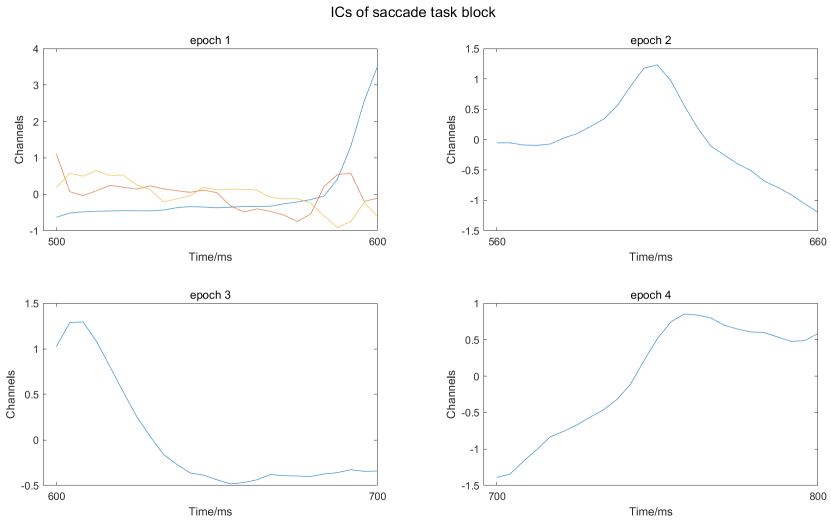

(b)

Figure 18: (a) ICs of Epochs in Target Onset Block (b) ICs of Epochs in Saccade Task Block

crease in correlation enhance the performance of locating the current generators. To ensure the correlation in local scale more precise and general, we abandon the first time epoch in target onset block and the first time epoch in saccade task block, then we come up with the correlation in average of the rest epochs.

Table 2: Similarity between Original and Reconstructed CSD on BL071717

Similarity between Original and Reconstructed CSD	
reconstructed by all ICs	0.9702
reconstructed by selected ICs	0.5365

4.2.4 Supplemental Experiments

In this section, extra several datasets will be analyzed to prove the regulation and template concluded from the previous section.

4.2.4.1 BB080415 This dataset is from another monkey performing the same Target-Saccade Task. To analyze this dataset, it is possible to see whether the regulation and template concluded could employed on other units consistently.

Going through Figure 19-Figure 24, it is evident that even for another brand new unit, the ICA-Clustering methodology owns equivalent ability to locate the source generators. At the meanwhile, the three-stage template of performing task has proven to suitable for the new monkey as well. In Table 3, the correlation shows an analogous outcome.

Table 3: Similarity between Original and Reconstructed CSD on BB080415

Similarity between Original and Reconstructed CSD	
reconstructed by all ICs	0.9683
reconstructed by selected ICs	0.5052

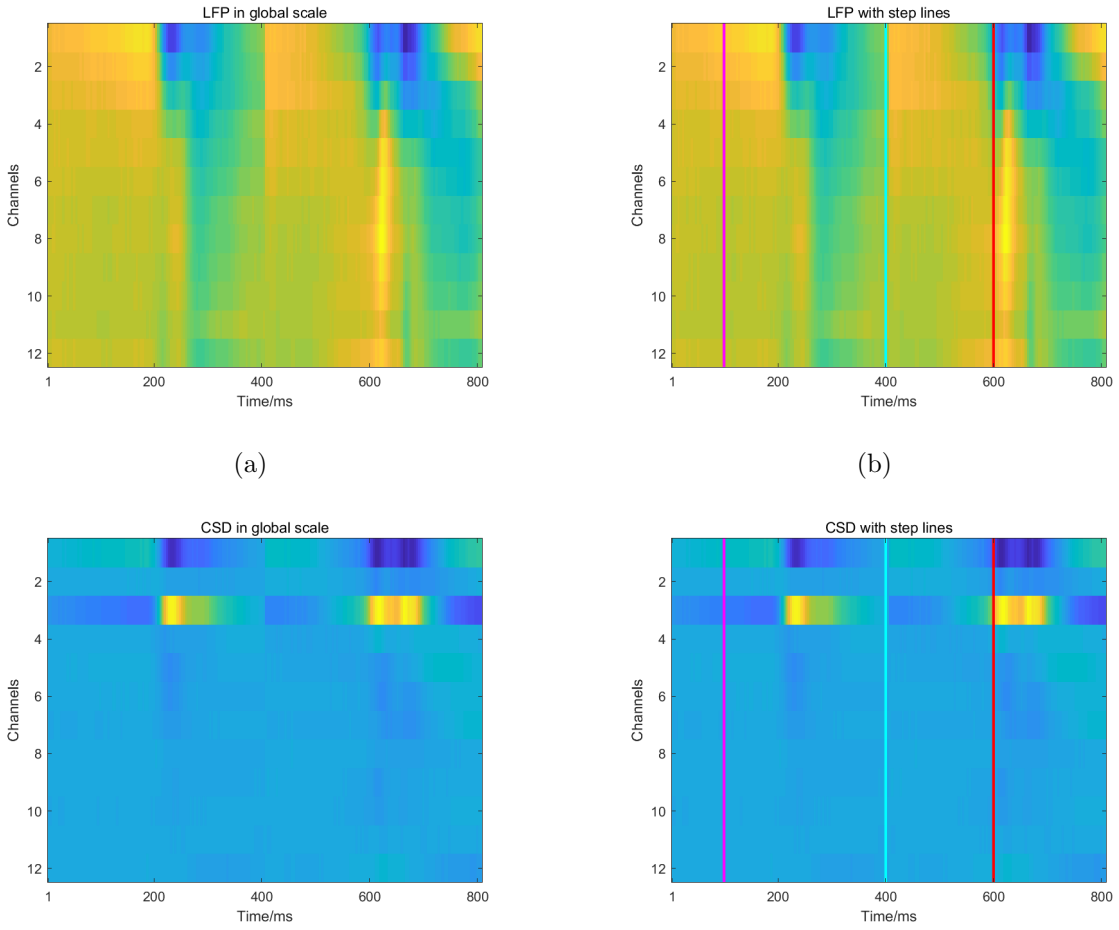

Figure 19: (a) LFP of Dataset (b) LFP of Dataset with Step Lines (C) CSD of Dataset (d) CSD of Dataset with Step Lines

(a)

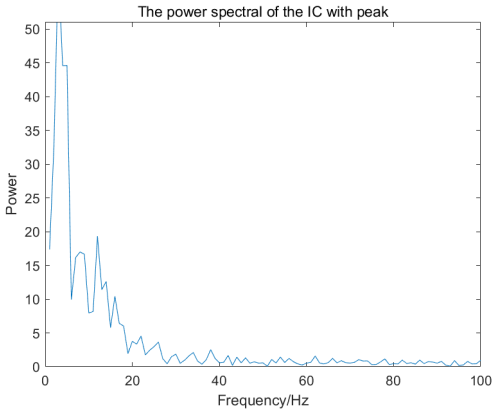

(b)

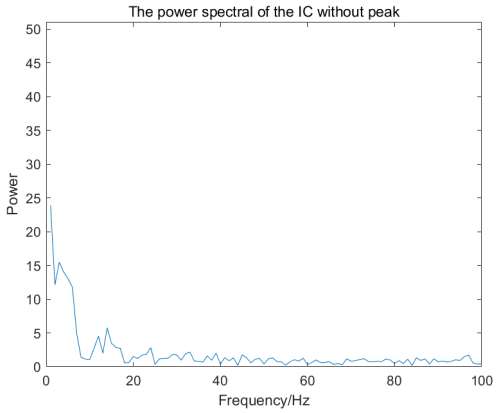

(c)

Figure 20: (a) Independent Components in Global Scale (b) Spectral Power of Peaking IC (c) Spectral Power of Residual IC

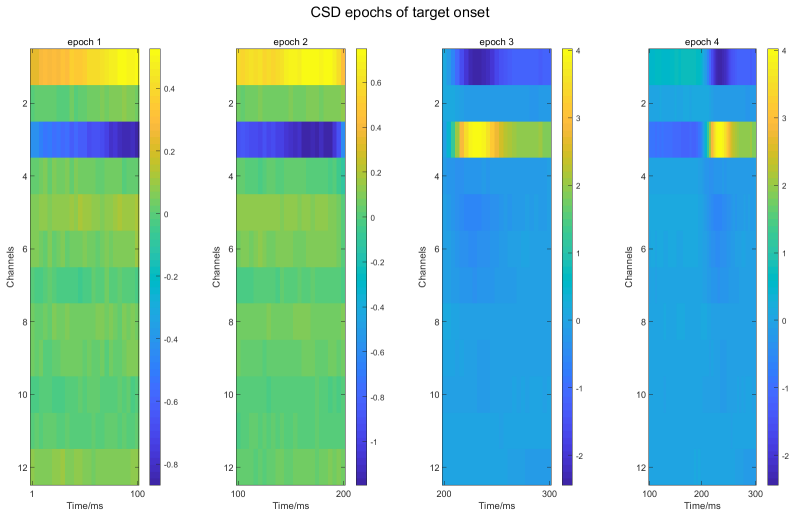

(a)

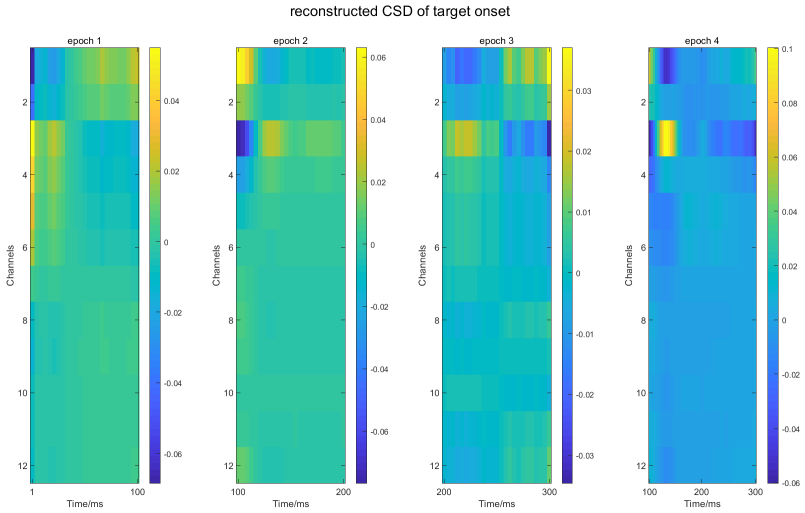

(b)

Figure 21: (a) CSD epochs of target onset block (b) reconstructed CSD epochs of target onset block

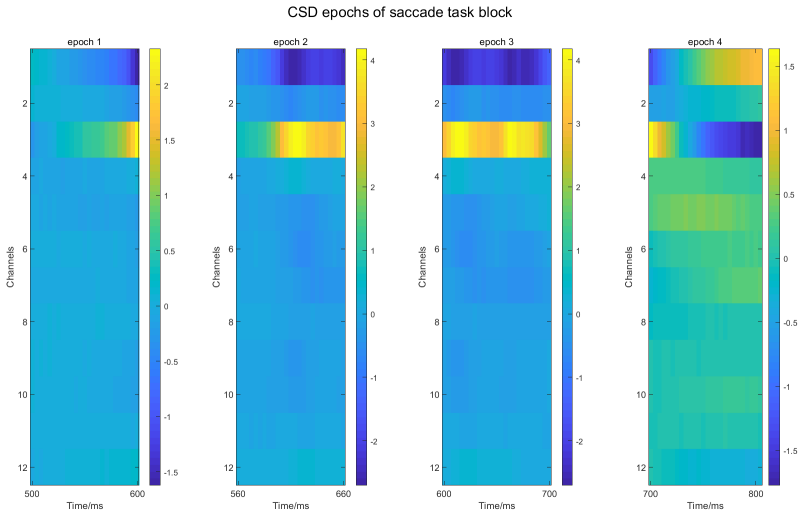

(a)

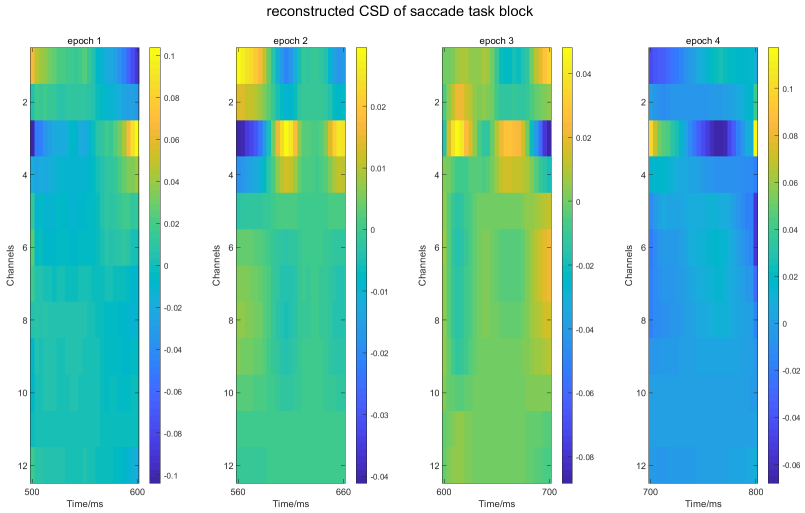

(b)

Figure 22: (a) CSD epochs of saccade task epochs (b) reconstructed CSD epochs of saccade task block

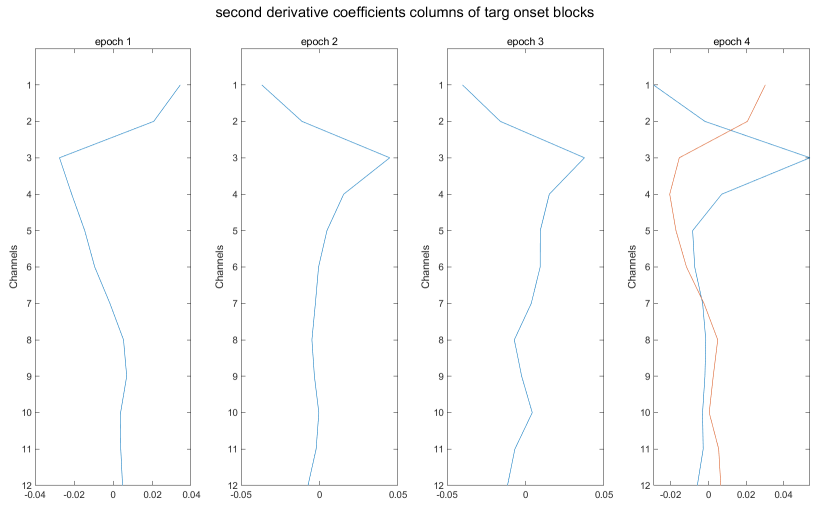

(a)

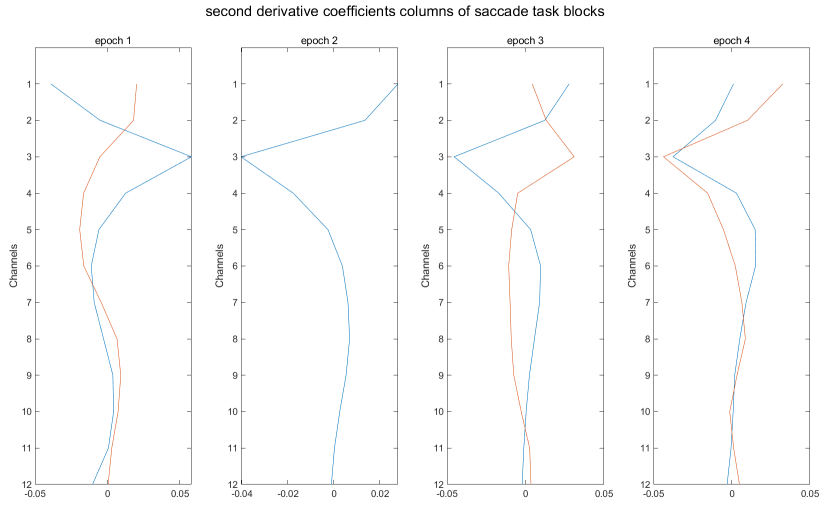

(b)

Figure 23: (a) 2^{nd} Derivative Coefficients of Epochs in Target Onset Block (b) 2^{nd} Derivative Coefficients of Epochs in Saccade Task Block

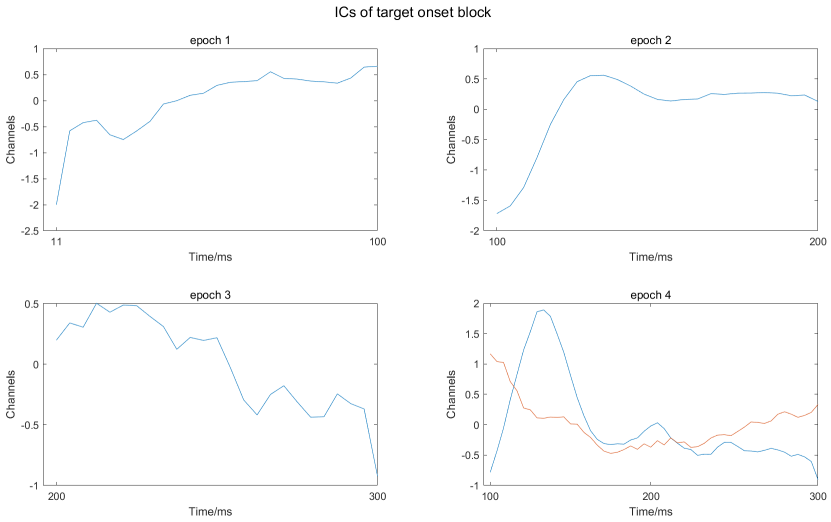

(a)

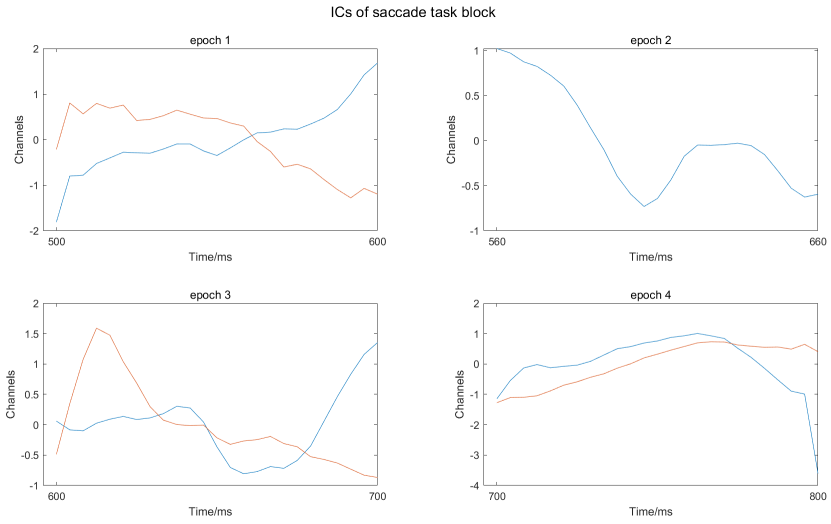

(b)

Figure 24: (a) ICs of Epochs in Target Onset Block (b) ICs of Epochs in Saccade Task Block

4.2.4.2 BU080918 Here, Figure 25-Figure 30, it will exhibit the results of another new monkey performing the same task, which do certainly have a similar performance comparing to the previous two monkeys. In Table 4, the correlation shows an analogous outcome as well.

Table 4: Similarity between Original and Reconstructed CSD on BU080918

Similarity between Original and Reconstructed CSD	
reconstructed by all ICs	0.9576
reconstructed by selected ICs	0.4675

4.3 Conclusion and Future Work

4.3.1 Conclusion

In the thesis, we employ ICA on the simulation data and our real sets to extract the mathematical objects, independent components and the corresponding mixing matrix, to realize our own generators locating approach. To find the loci of generators hidden, we use second derivative of selected mixing columns, computed with a Laplacian of Gaussian kernel, to multiply the corresponding independent components to reconstruct the CSD signals. We select those mixing columns and their corresponding independent components by a dedicated clustering algorithm based on correlation. In the end, the clustering algorithm gives back 1-3 selected components, which act as major roles during the repeated bootstrapping, mostly confined near the boundary of superficial and intermediate layers. The strongest modulations occurred slightly after saccade onset and in response to target onset. It discover a template about how the sensory signals in the superficial layers transform to motoric signals in the middle layers. Once the target onset in the screen, the monkey's brain is stimulated and a long-lasting response has shown in the superficial channel, and this response decays with time gradually. Then we can see in the saccade task part, with eye movement behavior

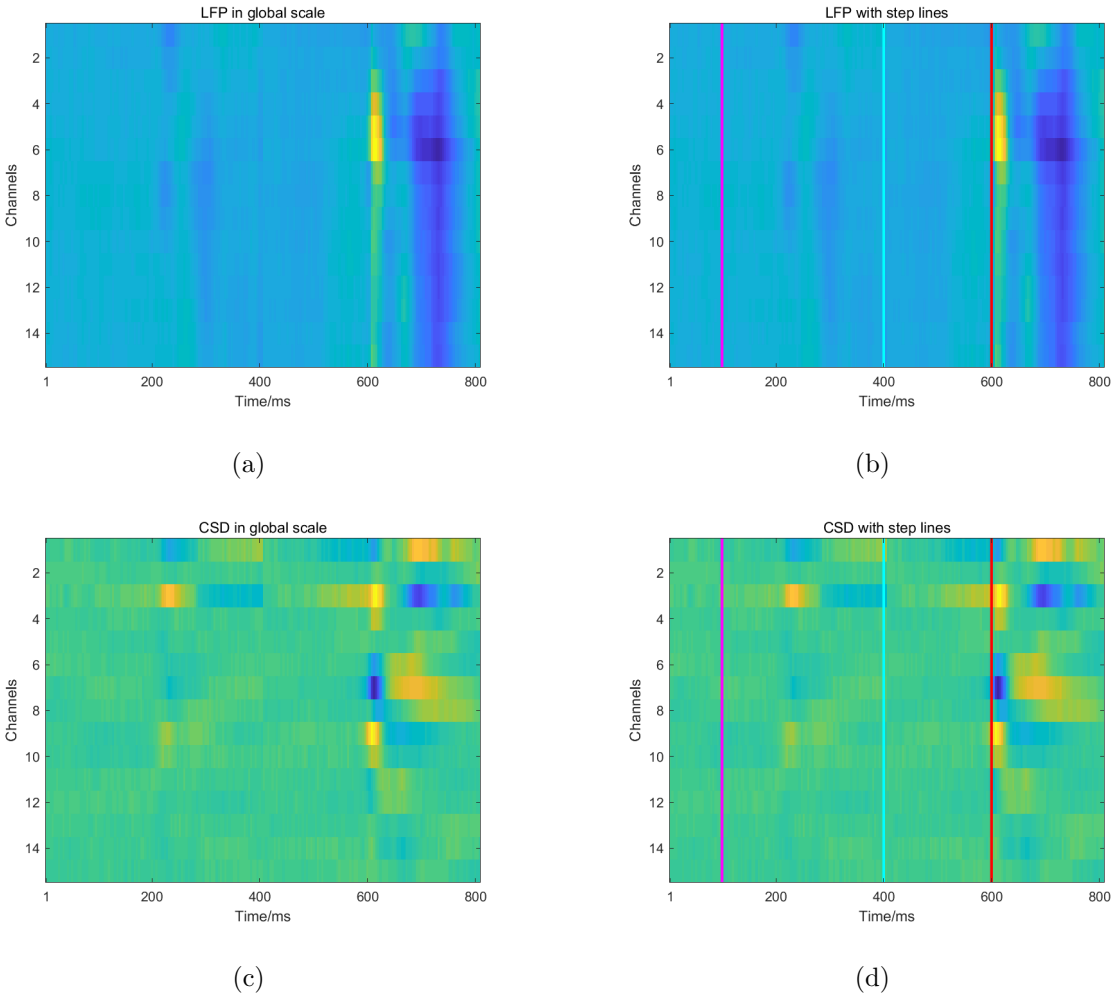

Figure 25: (a) LFP of Dataset (b) LFP of Dataset with Step Lines (C) CSD of Dataset (d) CSD of Dataset with Step Lines

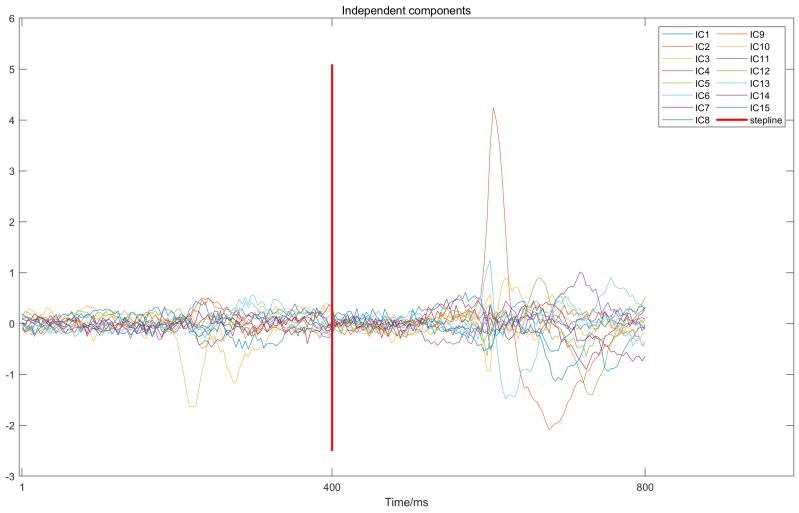

(a)

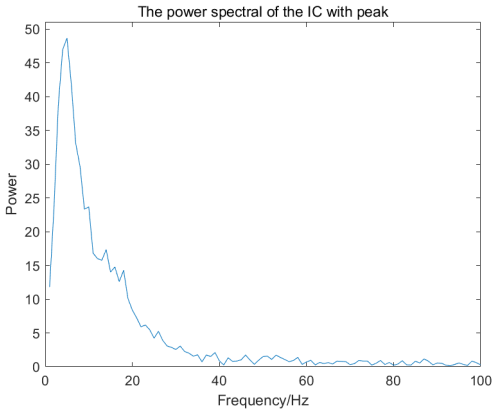

(b)

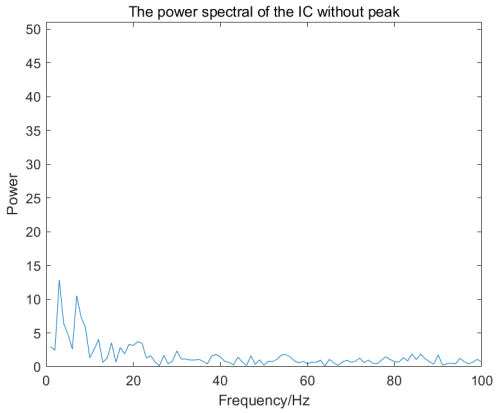

(c)

Figure 26: (a) Independent Components in Global Scale (b) Spectral Power of Peaking IC (c) Spectral Power of Residual IC

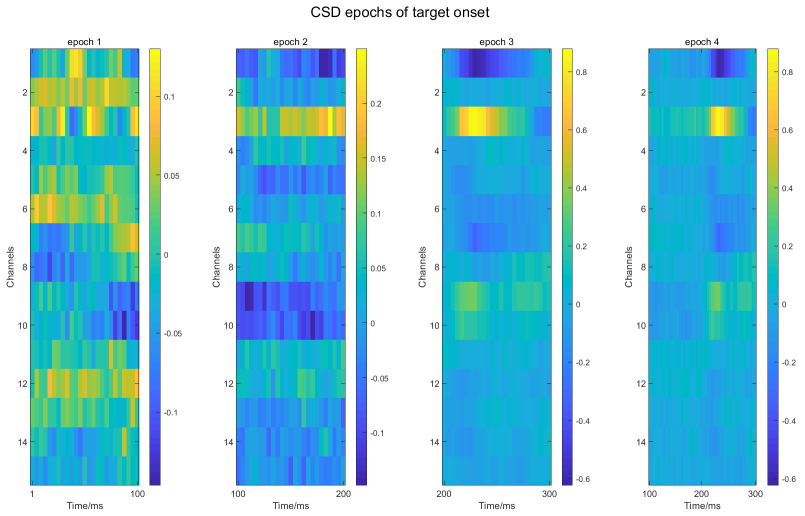

(a)

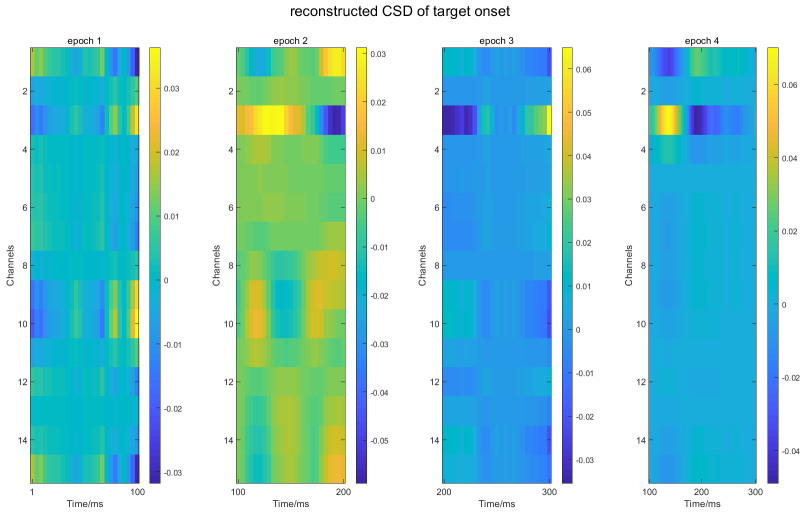

(b)

Figure 27: (a) CSD epochs of target onset block (b) reconstructed CSD epochs of target onset block

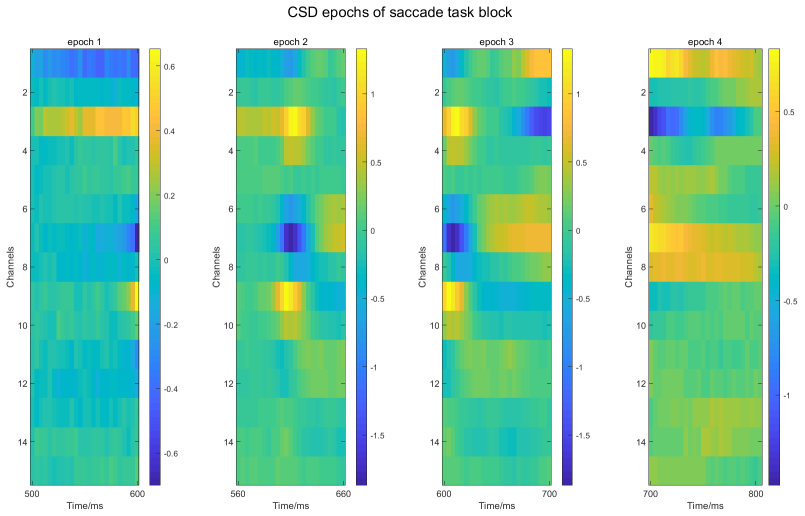

(a)

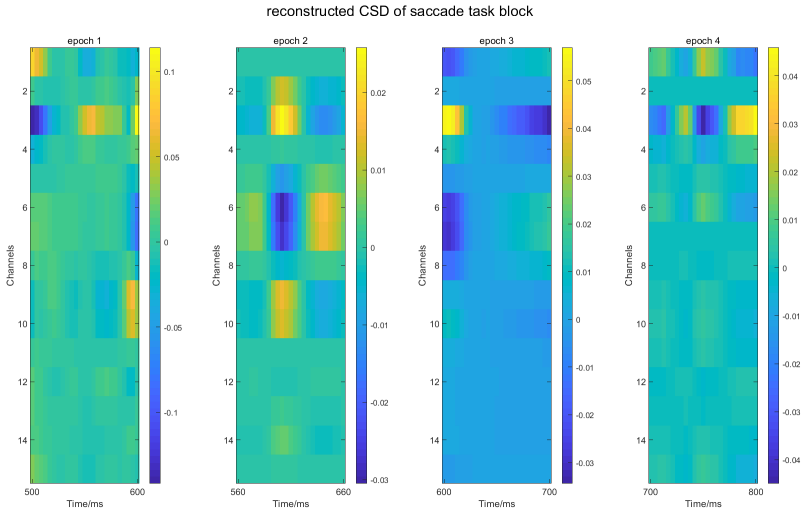

(b)

Figure 28: (a) CSD epochs of saccade task epochs (b) reconstructed CSD epochs of saccade task block

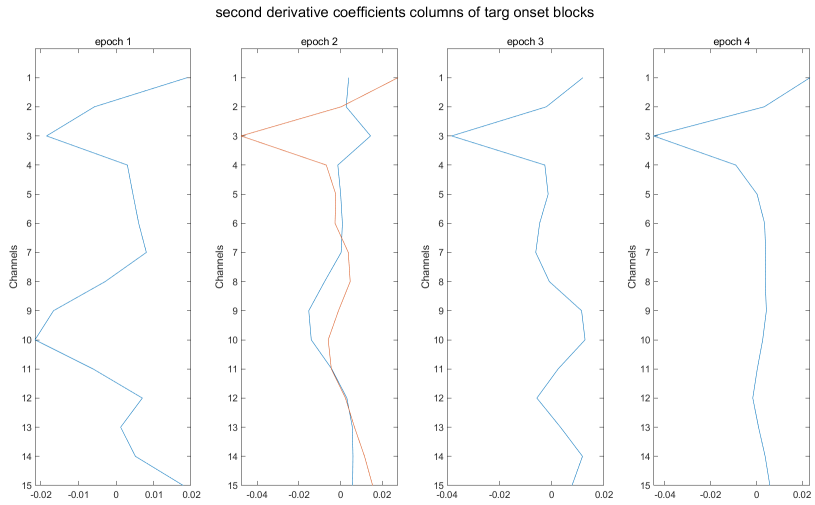

(a)

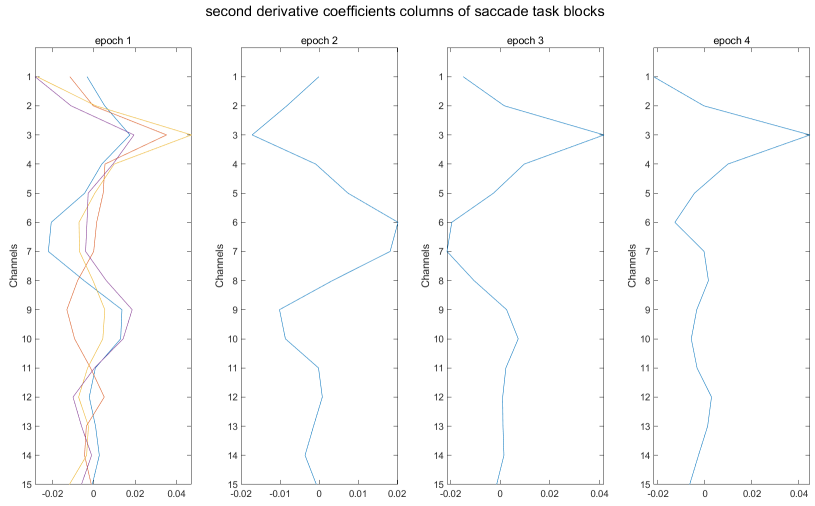

(b)

Figure 29: (a) 2^{nd} Derivative Coefficients of Epochs in Target Onset Block (b) 2^{nd} Derivative Coefficients of Epochs in Saccade Task Block

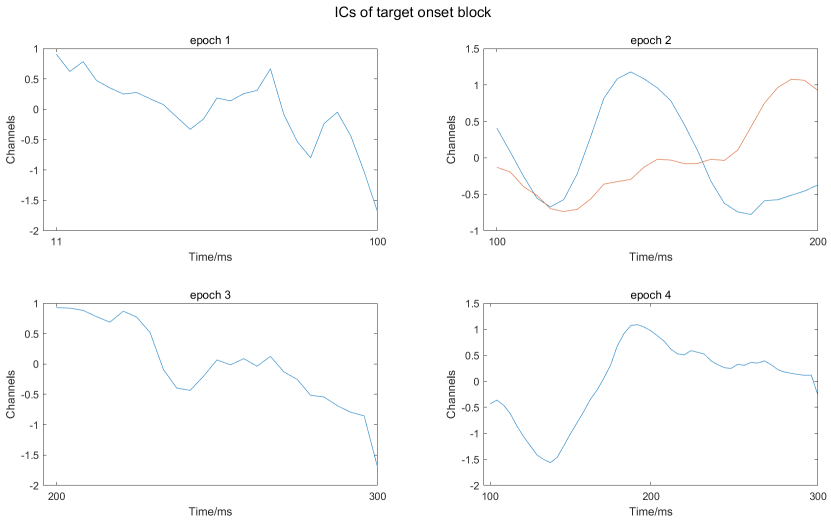

(a)

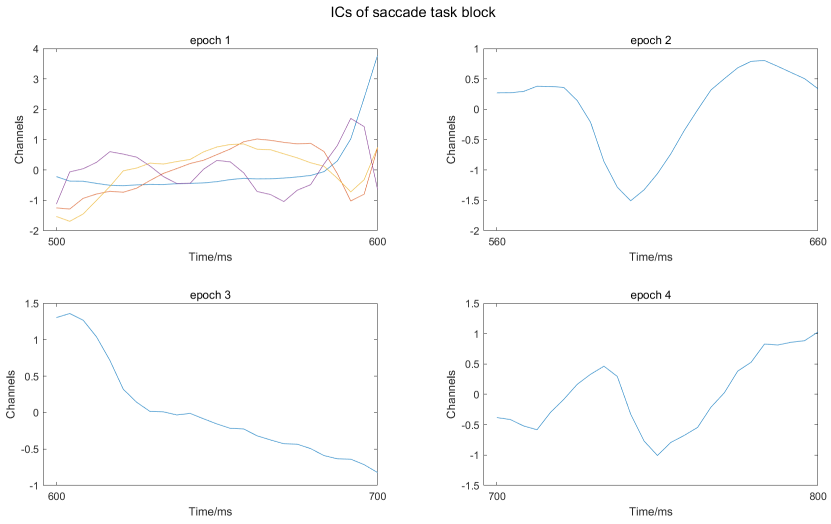

(b)

Figure 30: (a) ICs of Epochs in Target Onset Block (b) ICs of Epochs in Saccade Task Block

performing, there shows to be an obvious transmission from superficial channels to the deeper channels. The transmission is also decaying with time passing. At the end of eye movement task, the response returned to be only detected in superficial, just as the states in target onset. Then we compare our reconstruction against the traditional CSD analysis, which relies on the finite numerical approximation. Although our approach might consume a little more time, our reconstruction could show loci of the generators more clearly, get ridding of volume noise, which indicates our ICA-clustering methodology can accurately, if not better, reconstruct the CSD to identify and quantify the origin of current sinks.

4.3.2 Future Work

For a deep study in neuron communication, it is not enough to consider the LFP in low frequency plane. It will benefit a lot to relate the LFP in low frequency plane and the spikes in high frequency plane, which means a spike-coherence analysis could applied in the future work.

Bibliography

[1] R. Caton, "The electric currents of the brain," *Br Med J*, vol. 2, p. 278, 1875.

[2] W. Pitts, "Investigations on synaptic transmission," in *Cybernetics, Trans. 9th Conf. Josiah Macy, New York*, 1952, pp. 159–162.

[3] C. Nicholson and J. A. Freeman, "Theory of current source-density analysis and determination of conductivity tensor for anuran cerebellum," *Journal of neurophysiology*, vol. 38, no. 2, pp. 356–368, 1975.

[4] J. Freeman and C. Nicholson, "Experimental optimization of current source-density technique for anuran cerebellum," *Journal of neurophysiology*, vol. 38, no. 2, pp. 369–382, 1975.

[5] U. Mitzdorf, "Current source-density method and application in cat cerebral cortex: investigation of evoked potentials and eeg phenomena," *Physiological reviews*, vol. 65, no. 1, pp. 37–100, 1985.

[6] G. Buzsáki, "Large-scale recording of neuronal ensembles," *Nature neuroscience*, vol. 7, no. 5, p. 446, 2004.

[7] J. Du, T. J. Blanche, R. R. Harrison, H. A. Lester, and S. C. Masmanidis, "Multiplexed, high density electrophysiology with nanofabricated neural probes," *PloS one*, vol. 6, no. 10, p. e26204, 2011.

[8] G. T. Einevoll, C. Kayser, N. K. Logothetis, and S. Panzeri, "Modelling and analysis of local field potentials for studying the function of cortical circuits," *Nature Reviews Neuroscience*, vol. 14, no. 11, p. 770, 2013.

[9] W. Rall and G. M. Shepherd, "Theoretical reconstruction of field potentials and dendrodendritic synaptic interactions in olfactory bulb." *Journal of neurophysiology*, vol. 31, no. 6, pp. 884–915, 1968.

[10] A. D. Protopapas, M. Vanier, and J. M. Bower, "Simulating large networks of neurons," *Methods in neuronal modeling: From ions to networks*, p. 461, 1998.

[11] P. L. Nunez, R. Srinivasan *et al.*, *Electric fields of the brain: the neurophysics of EEG*. Oxford University Press, USA, 2006.

[12] C. Gold, D. A. Henze, C. Koch, and G. Buzsaki, "On the origin of the extracellular action potential waveform: a modeling study," *Journal of neurophysiology*, vol. 95, no. 5, pp. 3113–3128, 2006.

[13] K. H. Pettersen and G. T. Einevoll, "Amplitude variability and extracellular low-pass filtering of neuronal spikes," *Biophysical journal*, vol. 94, no. 3, pp. 784–802, 2008.

[14] C. Bédard, H. Kröger, and A. Destexhe, "Modeling extracellular field potentials and the frequency-filtering properties of extracellular space," *Biophysical journal*, vol. 86, no. 3, pp. 1829–1842, 2004.

[15] C. Bédard and A. Destexhe, "Local field potential interaction with the extracellular medium," *Encyclopedia of Computational Neuroscience*, pp. 1540–1547, 2015.

[16] M. Hämäläinen, R. Hari, R. J. Ilmoniemi, J. Knuutila, and O. V. Lounasmaa, "Magnetoencephalography—theory, instrumentation, and applications to noninvasive studies of the working human brain," *Reviews of modern Physics*, vol. 65, no. 2, p. 413, 1993.

[17] W. Denk, K. R. Delaney, A. Gelperin, D. Kleinfeld, B. Strowbridge, D. W. Tank, and R. Yuste, "Anatomical and functional imaging of neurons using 2-photon laser scanning microscopy," *Journal of neuroscience methods*, vol. 54, no. 2, pp. 151–162, 1994.

[18] Y. Nir, R. J. Staba, T. Andrillon, V. V. Vyazovskiy, C. Cirelli, I. Fried, and G. Tononi, "Regional slow waves and spindles in human sleep," *Neuron*, vol. 70, no. 1, pp. 153–169, 2011.

[19] D. Contreras and M. Steriade, "Cellular basis of eeg slow rhythms: a study of dynamic corticothalamic relationships," *Journal of Neuroscience*, vol. 15, no. 1, pp. 604–622, 1995.

[20] G. Buzsaki, M. Penttonen, Z. Nadasdy, and A. Bragin, "Pattern and inhibition-dependent invasion of pyramidal cell dendrites by fast spikes in the hippocampus in vivo," *Proceedings of the National Academy of Sciences*, vol. 93, no. 18, pp. 9921–9925, 1996.

[21] G. Buzsáki, C. A. Anastassiou, and C. Koch, "The origin of extracellular fields and currents—eeg, ecog, lfp and spikes," *Nature reviews neuroscience*, vol. 13, no. 6, p. 407, 2012.

[22] D. K. Wójcik, "Current source density (csd) analysis," *Encyclopedia of Computational Neuroscience*, pp. 915–922, 2015.

[23] J. V. Tranquillo, "Quantitative neurophysiology," *Synthesis Lectures on Biomedical Engineering*, vol. 3, no. 1, pp. 1–142, 2008.

[24] K. H. Pettersen, A. Devor, I. Ulbert, A. M. Dale, and G. T. Einevoll, "Current-source density estimation based on inversion of electrostatic forward solution: effects of finite extent of neuronal activity and conductivity discontinuities," *Journal of neuroscience methods*, vol. 154, no. 1-2, pp. 116–133, 2006.

[25] D. R. Kipke, W. Shain, G. Buzsáki, E. Fetz, J. M. Henderson, J. F. Hetke, and G. Schalk, "Advanced neurotechnologies for chronic neural interfaces: new horizons and clinical opportunities," *Journal of Neuroscience*, vol. 28, no. 46, pp. 11 830–11 838, 2008.

[26] L. Berdondini, P. Van Der Wal, O. Guenat, N. F. de Rooij, M. Koudelka-Hep, P. Seitz, R. Kaufmann, P. Metzler, N. Blanc, and S. Rohr, "High-density electrode array for imaging in vitro electrophysiological activity," *Biosensors and bioelectronics*, vol. 21, no. 1, pp. 167–174, 2005.

[27] A. Hyvärinen and E. Oja, "Independent component analysis: algorithms and applications," *Neural networks*, vol. 13, no. 4-5, pp. 411–430, 2000.

[28] C. Massot, U. K. Jagadisan, and N. J. Gandhi, "Time-course of population activity along the dorsoventral extent of the superior colliculus during delayed saccade tasks," *bioRxiv*, p. 571307, 2019.